JGR Planets

RESEARCH ARTICLE
10.1029/2023JE008177

Key Points:

- Isostatic compensation: We use the elastic thickness of the lithosphere to account for isostatic compensation in basin formation models
- Isostatic compensation of lunar farside basins varies with impactor size and thermal state, affecting basin's gravity signatures
- The effects of isostatic compensation on the estimated impactor sizes for farside basins are limited

Supporting Information:

Supporting Information may be found in the online version of this article.

Correspondence to:

T. Lompa,
tomke.lompa@mfn-berlin.de

Citation:

Lompa, T., Ebbing, J., & Wünnemann, K. (2024). Evolution of impact basin gravity signatures on the lunar farside: A long-term alteration process. *Journal of Geophysical Research: Planets*, *129*, e2023JE008177. https://doi.org/10.1029/2023JE008177

Received 22 OCT 2023
Accepted 19 MAR 2024

Evolution of Impact Basin Gravity Signatures on the Lunar Farside: A Long-Term Alteration Process

T. Lompa[1,2], J. Ebbing[3], and K. Wünnemann[1,2]

[1]Department Solar Systems, Impacts and Meteorites, Leibniz-Institute for Evolution and Biodiversity Science, Museum für Naturkunde, Berlin, Germany, [2]Institute of Geological Sciences, Freie Universität Berlin, Berlin, Germany, [3]Institute of Geosciences, Satellite- and Aerogeophysics, Kiel University, Kiel, Germany

Abstract Lunar impact basins are critical markers to understand the early bombardment history. This study focuses on isostatic compensation processes at 16 lunar farside basins, exploring how long-term alteration processes affect estimates of impactor sizes and timing. Using a lithospheric flexure model, we analyze the isostatically compensated gravity signature of these basins. Our approach is based on previously published basin formation models using the iSALE-2D shock physics code. Here we investigate how isostatic compensation processes alter the gravity signature using models of basin formation as initial conditions. We compare our results with the present day observed gravity data. We assume that isostatic compensation is the result of flexural deformation of the crust-mantle boundary with varying lithospheric elastic thicknesses. Our results indicate that the effect of isostatic compensation on the gravity signature varies depending on the thermal conditions at the time of impact. We find that despite this variability, the overall influence of isostatic compensation on the gravity signature is generally moderate to minor. Additionally, our analysis is consistent with previous studies that have shown that the elastic thickness varies across the Moon. Our findings contribute to our understanding of the relationship between basin formation and the thermal evolution of the Moon. The variations in elastic thickness found provide nuanced insights into lunar geological processes and improve our understanding of the early history of the Moon.

Plain Language Summary This study addresses the early bombardment history of the Moon, particularly the basin forming asteroid impacts in the first 700 million years. The large crater structures and basins serve as historical markers that make it possible to estimate the size of the cosmic bodies that formed them and to estimate the thermal conditions of the Moon at the time of their formation. As the surface expression of some basins is poorly preserved, making size measurements uncertain, gravity anomalies, caused by subsurface mass displacements and changes in density, are valuable for evaluation. Based on previously published numerical simulations of basin formation, we correlate our results with gravity data from the Gravity Recovery and Interior Laboratory mission. In the period between the formation of the basin and today's observation, isostatic compensation processes probably caused changes that we are trying to reconstruct using models. Our findings emphasize the significant role of lithospheric elasticity, determining whether isostatic compensation occurs locally or regionally. Regarding the lunar farside, we observed spatial variations in elastic thickness, dependent on the cooling history of each basin. Importantly, our study revealed that previously determined impactor sizes exhibit no to minimal change with the introduction of isostatic compensation through our lithospheric flexure model.

1. Introduction

The Moon bears prominent scars from its violent early history. These are mainly seen as large impact basins that originated primarily within the first 700 million years after the Moon's formation (e.g., Morbidelli et al., 2012, 2018; Stöffler & Ryder, 2001; Wilhelms et al., 1987). Advancements in topographic satellite data, particularly from the Lunar Orbiter Laser Altimeter (LOLA) on the Lunar Reconnaissance Orbiter (Smith et al., 2010), made it possible to analyze the present-day morphology and morphometry of these basins. These measurements serve as constraints for estimating impactor sizes (e.g., Lompa et al., 2021a; Miljković et al., 2016), which then enables the reconstruction of the impactor flux during the early bombardment history of the inner solar system.

As subsequent impact events have degraded the surface expression of basins, the characteristic bulls-eye gravity signature, associated with an uplifted crust-mantle boundary (CrMB), has been proposed as a more suitable

measure of basin size (e.g., Lompa et al., 2021a; Miljković et al., 2016; Neumann et al., 2015; Potter et al., 2013; Wahl et al., 2020). High-resolution gravity data from the Gravity Recovery and Interior Laboratory (GRAIL) mission (Zuber et al., 2013) have been used to constrain numerical models of basin formation (e.g., Johnson et al., 2016; Zhu et al., 2015), as these models estimate the topography of the CrMB and can be directly compared to crustal thickness models (Wieczorek et al., 2013).

However, long-term alteration processes, such as viscoelastic relaxation and cooling after impact should be considered as well, which have affected the present-day CrMB and gravity signature. A key element in understanding basin relaxation is the viscosity of the lithosphere (e.g., Kamata et al., 2015; Mohit & Phillips, 2006), directly affected by the pre-impact thermal state of the basin (e.g., Conrad et al., 2018; Kamata et al., 2015). However, Kamata et al. (2013) demonstrated that temperatures with near-surface gradients below 20 K/km do not yield significant viscous relaxation.

In previous studies it was shown that relaxation processes in impact structures formed in a hot target involve viscous creep of lower crustal material, resulting in a flattening of the CrMB (e.g., Solomon et al., 1982). In contrast, combining hydrocode modeling of crater formation and finite element (FE) modeling for long-term cooling and relaxation (Ding & Zhu, 2022; Freed et al., 2014; Melosh et al., 2013; Montesi, 2013), have shown that structures formed in a cold target retain their shape through isostatic balancing via basin uplift. Here, we analyze basins on the farside of the Moon, where relatively cold temperature profiles can be expected (Lompa et al., 2021a, Figure 1 therein) (Figure A1). Hence, we neglect the viscous relaxation part and apply a lithospheric flexure model.

Post-impact relaxation processes can be described using the elastic thickness (T_e) of the lithosphere, a measure commonly employed to indicate lithospheric strength (e.g., Burov & Diament, 1995; Crosby & McKenzie, 2005; Goossens et al., 2022). This parameter reflects factors such as the thermal state of the lithosphere (e.g., Spohn et al., 2001; Tosi et al., 2015), the state of the CrMB, and the thickness of the competent crust and mantle (e.g., Burov & Diament, 1995).

For example, variations in crust and mantle thickness directly control topographic and internal loads, leading to flexure processes in basin regions and changes in the isostatic state (e.g., Burov & Diament, 1995; Huang & Wieczorek, 2012). Sugano and Heki (2004) noted that during the Moon's cooling history, the lunar lithospheric thickness increased (Spohn et al., 2001), implying that most isostatic responses occurred shortly after basin formation. Previous studies (e.g., Crosby & McKenzie, 2005; Huang & Wieczorek, 2012; Sugano & Heki, 2004; Z. Zhong et al., 2018) have used admittance analyzes between GRAIL gravity data (Zuber et al., 2013) and LOLA topographic data (Smith et al., 2010) to determine selenophysical parameters, such as surface and subsurface loads, crustal thickness and density, and elastic thickness. These studies have revealed variations in the elastic thickness of the Moon depending on the basin location and the time of basin formation, which reflects the cooling history of the Moon. Nevertheless, it is important to note that the loading assumptions may differ among these studies.

In contrast to prior studies focusing on individual impact structures, our research takes a comprehensive approach, analyzing the entire basin record on the lunar farside adopting a process-oriented gravity modeling approach (POGM) (e.g., Karner et al., 2005; Watts, 2018).

Based on previously conducted numerical models of the formation of 16 basins (Lompa et al., 2021a), taking into account varying impactor size and the thermal state of the lithosphere, in this study, we investigate isostatic compensation associated with the elastic thickness of the lithosphere (T_e). From these isostatic models, we select the best-fit scenarios by comparing the gravity signatures for 16 lunar farside basins to the observed gravity data. This allows us to estimate the impactor size responsible for the formation of a given basin at the time of impact, under the assumption that it is related to the thermal state of the lithosphere upon impact.

2. Methods

To investigate the effect of isostatic processes on observed basin structures, we employed a process-oriented gravity modeling (Section 2.2) approach to determine isostatically compensated best-fit models for selected impact structures on the lunar farside (black dots in Figure 1). We selected basins on the lunar farside without mare infilling, which have a positive anomaly in their center and are surrounded by a gravity low (Lompa et al., 2021a). Comparable structures can be found on the near side as well, but most of them are located in mare areas having a more complex mass distribution. As an exception, we included the frequently studied basin

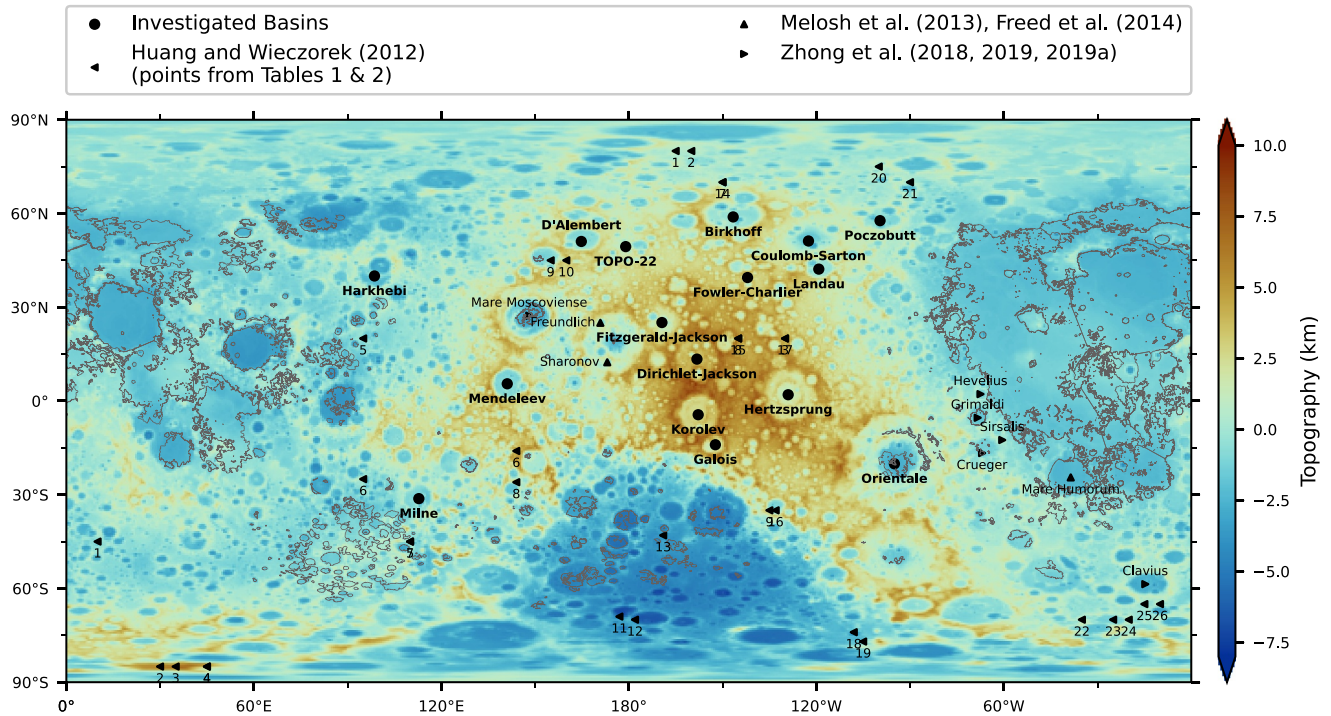

Figure 1. Topographic map of the Moon (MoonTopo2600p model from Wieczorek (2015)) in Plate Carrée projection centered on the farside at 180° longitude, created with SHTools (Wieczorek & Meschede, 2018; Wieczorek et al., 2022). Basins investigated in this study are shown with black dots. Locations investigated by others: Huang and Wieczorek (2012) (triangle left), Freed et al. (2014) and Melosh et al. (2013) (triangle up), and Z. Zhong, Yan, Alexis, and Rodriguez (2019), Z. Zhong, Yan, Zhang, et al. (2019), Z. Zhong et al. (2018) (triangle right). Contour lines indicate the mare locations (Nelson et al., 2014).

Orientale. Details of the dataset of formation models using the iSALE shock-physics code are stated in Lompa et al. (2021a). For the available formation models, we performed a flexure calculation (Section 2.1) for the lithosphere using the software GMT (Wessel et al., 2019) with the elastic thickness as a free parameter. In a last step of our process-oriented modeling (Section 2.2), we carried out a dynamic warping (DW) analysis as in Lompa et al. (2021a) to determine the isostatically compensated model (ICM) with the best agreement of observed and modeled gravity signature. As a quantitative measure of the quality of the fit between our models and the observed data, we determined the normalized root-mean squared error (*NRMSE*).

2.1. Flexural Isostasy

The formation of lunar basins occurred at different times, which means that the thermal conditions varied during the basin formation. The bending of the lithosphere depends on its composition and flexural rigidity, which, in turn, is influenced by the thermal structure (e.g., Turcotte & Schubert, 2002). Consequently, a thin and warm crust will exhibit more bending compared to a cold and thick crust. The strength of the lithosphere plays an important role in the study of isostatic processes. The elastic thickness of the lithosphere is commonly used as a measure of its strength, which we treat as a free parameter. Isostasy models, affected by forces from an elastic mantle that bends under the load of the crust, transmit buoyant forces across a large region of deformation (Meinesz, 1939). In contrast to the local isostasy models proposed by Airy-Heiskanen and Pratt, which describe hydrostatic buoyancy without considering material strength, the isostasy model after Vening-Meinesz compensates topographic loads at a regional scale by balancing horizontal and vertical stresses for a homogeneous, elastic plate over a viscous mantle.

To determine the regional, isostatic behavior in our numerical models, we examine the effective elastic thickness (T_e). T_e is directly related to the flexural rigidity (D) of the plate, which also serves as a proxy for long-term strength (Watts, 2018). The flexural rigidity is defined as

$$D = \frac{ET_e^3}{12(1-\nu^2)}, \tag{1}$$

Table 1
Summary of Parameters Used in Flexure Calculations in GMT

Symbol	Parameter	Value
Z	Depth of compensation surface	100 km
T_e	Elastic thickness	Range: 0–200 km
		0–20 km: step size 5 km
		20–50 km: step size 10 km
		50–200 km: step size 20 km
ρ_m	Mantle density	3,314 kg m^{-3}
ρ_c	Crustal density	2,650–2,950 kg m^{-3} in 100 kg m^{-3} steps
E	Young's modulus	70 GPa
ν	Poisson's ratio	0.25
R	Average radius of the Moon	1,734.4 km
g	Gravity acceleration at the radius of R	1.62 m s^{-2}

with Young's modulus E, and Poisson's ratio ν, which characterize the elastic properties of the lithosphere (e.g., Turcotte & Schubert, 2002) (Table 1).

For the flexure calculation, we set Young's modulus (E) to 70 GPa and Poisson's ratio (ν) to 0.25. These values approximate the average properties of the crustal and mantle materials in the basin formation models described in Lompa et al. (2021a). The elastic thickness (T_e) ranges from 0 to 200 km and crustal densities vary between 2,650 and 2,950 kg m^{-3} (Table 1).

To compute the flexural deformation of the CrMB, we use the *gmtflexure* tool from GMT (Wessel et al., 2019). The input, vertical loads (q), are calculated from the difference of a reference model (crustal thickness before basin formation, assumed to be either 40 km or 60 km (Lompa et al., 2021a)) and the undulation of CrMB resulting from our basin formation model. The load difference accounts for both the crustal density for each model (Lompa et al., 2021a) and the associated density contrast between the crust and the mantle. As the crustal volume remains constant, the contrast between the surface and mantle density controls flexure (similar to models of post-glacial rebound) and sets the crust and infill densities in GMT to 0 kg m^{-3} and the mantle density to 3,314 kg m^{-3} (Table 1). In GMT, flexure is calculated by solving the general flexural equation

$$D\frac{d^4}{d^4x}w(x) + P\frac{d^2}{d^2x}w(x) + \left(\rho_m - \rho_l\right)gw(x) = q(x), \tag{2}$$

where D represents rigidities, P denotes horizontal forces, ρ_m signifies mantle density, ρ_l represents load density, w corresponds to flexure, g signifies surface gravity at average radius of the Moon, and q is the load.

In our study, we neglect the far-field horizontal stress on individual basins ($P = 0$) and consider ρ_l already in the load differences. Therefore, the GMT flexure calculation is simplified and later solved for the flexure $w(x)$:

$$D\frac{d^4}{d^4x}w(x) + \rho_m g w(x) = q(x). \tag{3}$$

If the plate has no rigidity ($D = 0$ or $T_e = 0$ km), we obtain flexure values for local isostatic compensation.

In a final step, we adjust the depth of the CrMB in the numerical simulations based on the flexure values. During this process, we maintain a constant mass in the crust by keeping the amount of crustal material unchanged while modifying the amount of mantle material between the CrMB and the depth of isostatic compensation. In this study, we refer to such models as "isostatically compensated models" (ICM).

Figure 2 schematically illustrates the effect of local isostatic compensation ($T_e = 0$ km) for a lunar basin. We assume that the pre-impact lunar crust and upper mantle are in isostatic equilibrium. The load of this model remains constant at a depth (Z) of 100 km (482 MPa) (Figure 2a). Models of basin formation and the resulting topography of

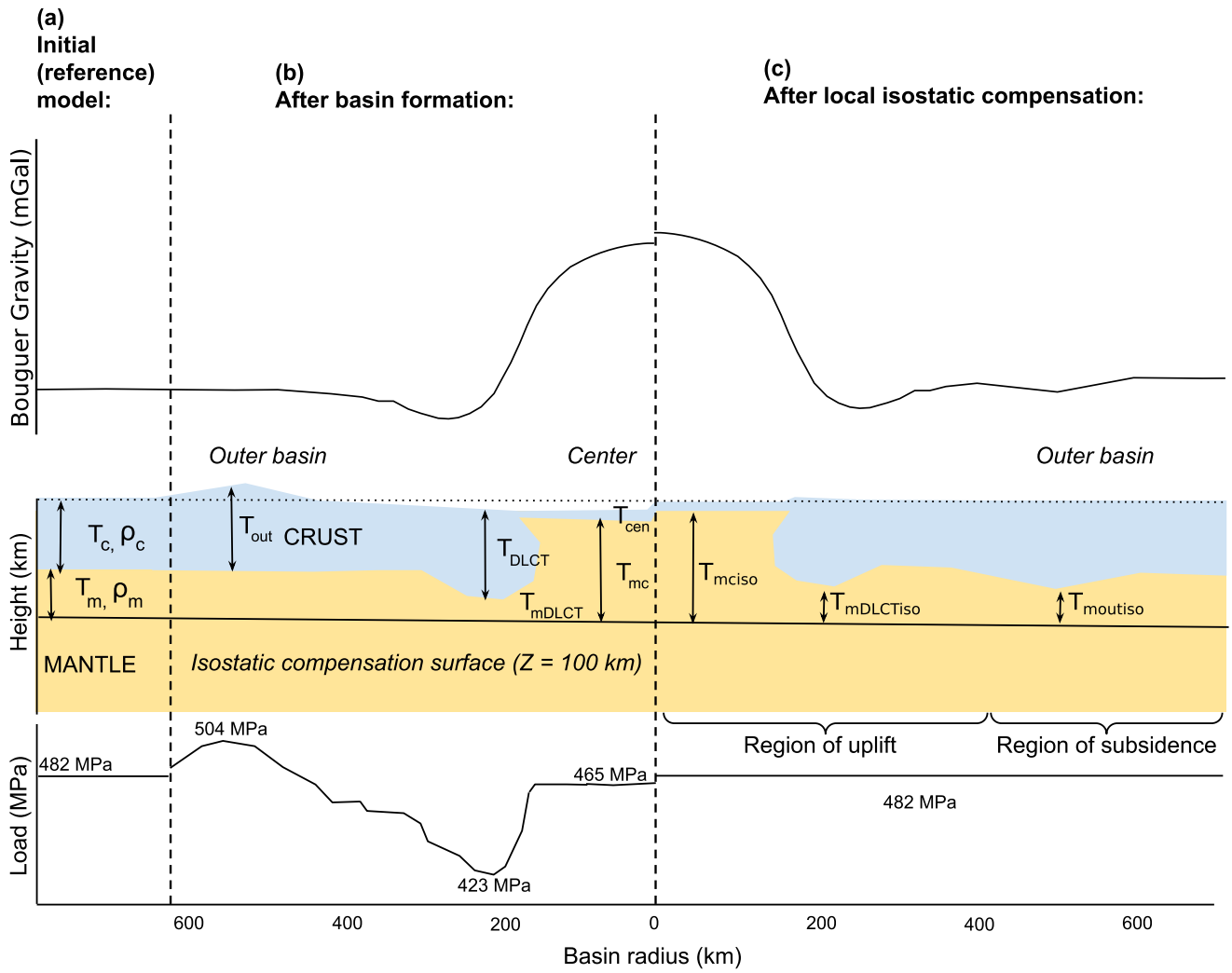

Figure 2. Concept of local isostatic adjustments in lunar basins ($T_e = 0$ km): (a) represents the reference model, showing the initial state of the lunar basin before the impact event, (b) depicts the basin structure immediately after the impact event, indicating the isostatic imbalance. (c) Demonstrates the model after isostatic compensation, where the basin has achieved a state of isostatic equilibrium. Below the model sections, we present the corresponding load profile, which is calculated up to the reference depth (Z) of 100 km. After isostatic compensation, the load of the compensated model (c) aligns with that of the reference model (a), indicating isostatic equilibrium. Above the sections, the corresponding Bouguer anomalies are shown.

the CrMB represent the isostatically uncompensated state immediately after impact, where dynamic motions have ceased on a time-scale of tens of minutes (Figure 2b). The corresponding load, calculated for a reference depth of 100 km, varies along the horizontal profile, indicating an isostatic imbalance. In regions with thickened crust (T_{DLCT}), the load is smaller than the reference load, while it is larger at the outer basin (T_{out}). Based on the load difference, the GMT flexure model determines the amount of uplift or subsidence of the CrMB by assuming a locally compensated model to obtain isostatic equilibrium. Generally, load variation indicates isostatic under- or overcompensation. Isostatic compensation for local isostasy ($T_e = 0$ km), modifies the basin structure as shown in Figure 2c. Alternatively, when the elastic thickness varies ($T_e > 0$ km), we achieve regional isostatic compensation. Higher values of T_e imply that the basin structure depicted in Figure 2b will not change significantly, but as T_e decreases, it converges to the structure illustrated in Figure 2c. To observe this effect, we refer to Figure 3 in the results section; Figure 2 only demonstrates the case for $T_e = 0$ km to illustrate the concept underlying this study.

2.2. Process-Oriented Gravity Modeling

We use Process-Oriented Gravity Modeling (POGM) to account for isostatic adjustment processes over time. In general, this form of modeling considers one or more geological processes, such as loading, along with the density

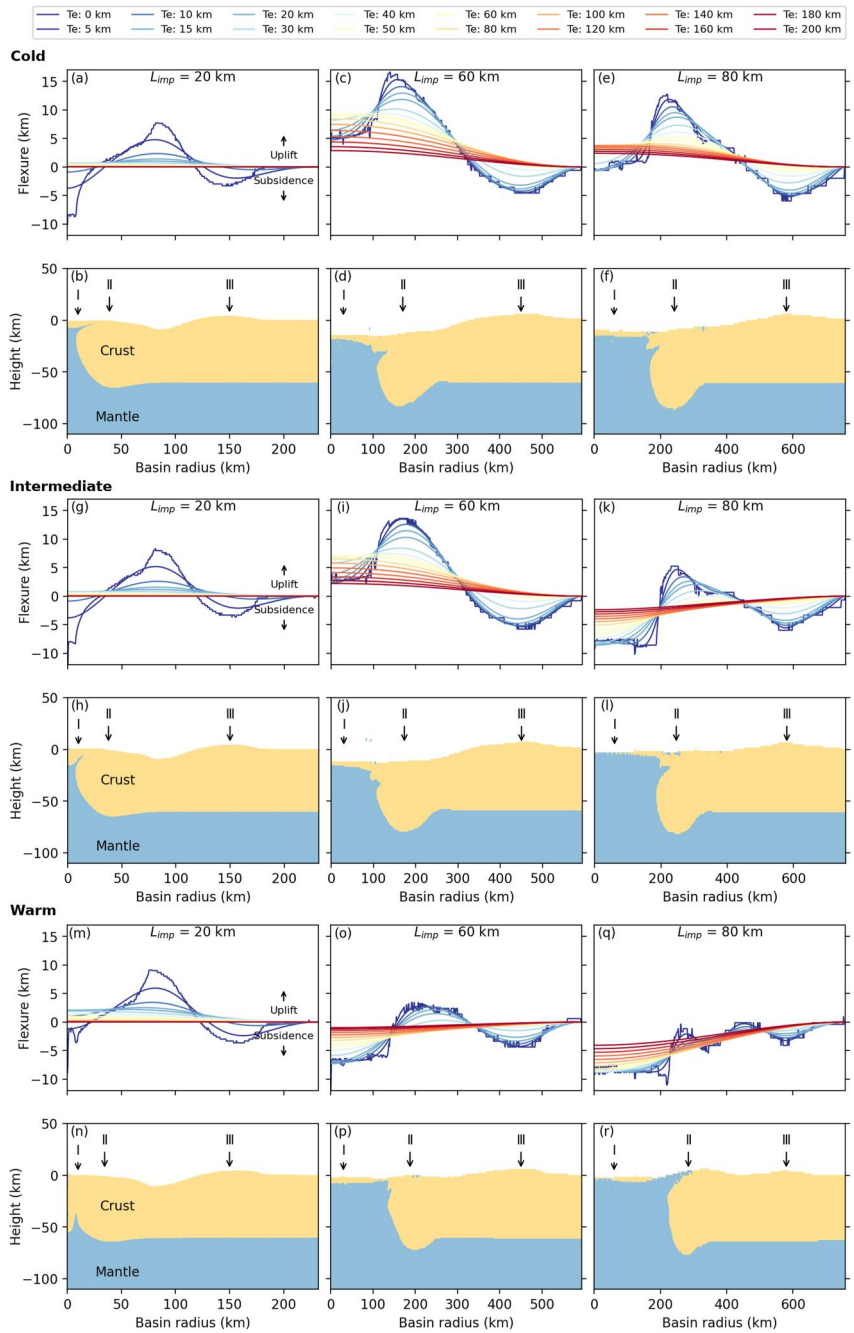

Figure 3. Sections through (uncompensated) iSALE models with thermal profiles categorized as cold (b, d, f), intermediate (h, j, l), and warm (n, p, r). The models feature a 60 km thick crust and impactor diameters of 20, 60, and 80 km. The corresponding flexural displacements for different elastic thicknesses are shown above (a, c, e; g, i, k; m, o, q). The flexure calculations consider a crustal density of 2,750 kg m^{-3}. Colors in the flexural displacement plots indicate the elastic thickness value, T_e. Specific numbers within the figure correspond to the following: (I) Basin center, (II) Location of 0.5 *DLCT* (*DLCT*-values taken from Table S1 in the Supplementary Information of Lompa et al. (2021a)), (III) Area outside the basin with additional load on top of the 60 km thick crust. Note: The height profiles are vertically exaggerated for visualization purposes.

of the source body which produces the gravity field. In POGM, parameters related to geological processes, such as the flexural rigidity of the lithosphere, are varied to achieve a good fit with the observed gravity anomalies. POGM takes into account the dynamic processes that have occurred in the past and seeks to incorporate them into the modeling procedure (e.g., Watts, 2018). In our modeling, we vary the values of T_e to determine the best-fit

model for the selected 16 lunar farside basins from a database of 54 formation models (see Lompa et al., 2021a) with an impactor size range of 20–100 km, two crustal thicknesses, and three different thermal profiles representing different formation ages.

In the first processing step, we calculate the Bouguer gravity anomaly following the procedure in Collins (2014) (for details, see their Supporting Information S1) by assuming four crustal densities (2,650 to 2,950 kg m^{-3} in 100 kg m^{-3} steps), which increases the total number of models in our database to 216. In the models, the mantle density remains constant at a value of 3,314 kg m^{-3}. To remove the influence of basin topography on the modeled gravity signal, we applied a Bouguer correction assuming the density of the crust. This correction ensures that the gravity signal primarily represents the density contrast between the crust and mantle, thus reflecting the shape of the CrMB.

We use 16 elastic thicknesses ($T_e = 0$–200 km) which extends the parameter space to a total number of 3,456 gravity models to be compared with the Bouguer anomaly of the 16 lunar basins to find the best fit and thus the most likely impactor size and formation age for a given basin. The calculation of the isostatic adjustment assuming different T_e-values is terminated (for $T_e \leq 200$ km) when the gravity signature does not change any further.

After deriving the gravity signatures of the ICM, we compare them with the Bouguer gravity signatures of the 16 lunar farside basins (Lompa et al., 2021a) from the GRAIL mission (Zuber et al., 2013). For the sake of consistency between this study and Lompa et al. (2021a), we used the data from Lompa et al. (2021a). There, we used the gravity field model from Zuber et al. (2013), developed to spherical harmonic degree and order of 1,500 (Park et al., 2015). The spatial resolution of the field is about 8 km. The profiles contain the azimuthally averaged data of each basin.

To evaluate the fit, we use the DW method as described in Lompa et al. (2021a). In general, DW is a technique for comparing and measuring the similarity between two signals (Müller, 2007, 2015). Compared to traditional quantitative correlation, which aims at minimizing the area between the two curves (small areas suggest a higher correlation between the signals), the DW-method enables an accurate comparison between the shape of the signals. In the DW-method the Euclidean distances between the measured and modeled signatures are calculated pointwise. As a result, we obtain a Euclidean distance matrix, which is then transferred to a cumulative distance matrix (e.g., Lompa et al., 2021a). This matrix quantitatively shows the similarity between the signatures represented by the color-coded distance values. The gravity data of the model with the highest similarity to the observed gravity data correspond to the best-fit model of a given basin. For further insights into the processing steps of the gravity data, which are required for the signature comparison and a detailed description of how the DW-method works, we refer to the Supplementary Information S1 (Text S6, Figure S8) from Lompa et al. (2021a).

To quantitatively assess the DW-matrix in order to find the best-fit model for each basin, we use the concept of the root-mean squared error (*RMSE*). The *RMSE* is defined by subtracting the elements of the DW-matrix from the elements of a reference DW-matrix using the absolute values, which leads to the difference matrix:

$$RMSE = \sqrt{MSE} = \sqrt{\frac{1}{N}\sum_{i=1}^{N}\left(y_{i_{Ref}} - y_{i_{modeled}}\right)^2} \tag{4}$$

The DW-matrix is based on the modeled gravity signature versus the observed signature of the basin for a defined crustal density (Equation 4, $y_{i_{modeled}}$). The reference DW-matrix represents the best-fit matrix for this basin and contains the distances comparing the observed gravity signature of a basin to itself (Equation 4, $y_{i_{Ref}}$). The *RMSE*-value here is not an error in a strict sense, but it serves as a measure of deviation between a best-fit model and a perfect fit to the reference case.

In a second step, we normalize the *RMSE* (*NRMSE*) to remove the scale dependency to allow for a comparison of errors of different sized basins. In Neumann et al. (2015) the contrast of the Bouguer anomaly (BA-contrast) correlates with the main ring basin diameter, and, thus, will be used here as a scaling for basin size to normalize the *RMSE*. Therefore, we divide the *RMSE* by the difference between the largest $\left(y_{GRAIL_{\max}}\right)$ and smallest $\left(y_{GRAIL_{\min}}\right)$ gravity values of the observed signature (BA-contrast):

$$NRMSE = \frac{RMSE}{y_{GRAIL_{max}} - y_{GRAIL_{min}}} \quad (5)$$

A small *NRMSE* value indicates a good fit; a value of zero would mean that the GRAIL and the signal from the basin formation model are identical.

In addition to the *NRMSE* values of the ICM, we determined the errors of our best-fit models from Lompa et al. (2021a) to compare the quality of the fits between the best-fit models previously proposed from Lompa et al. (2021a) and the best-fit models assuming isostatic compensation.

3. Results

The Bouguer gravity anomaly relies on the density contrast between crust and mantle and therefore its shape and amplitude are directly affected by changes in CrMB location. For this reason, we first present the general effect of flexure and isostatic compensation on our numerical models (Section 3.1). Then we reevaluate previous estimates from Lompa et al. (2021a) regarding the gravity signature of modeled basins for given impactor sizes and masses, and thermal state and age of the examined lunar farside basins (Section 3.2).

3.1. General Implications of Flexure and Isostatic Compensation on Numerical Models

3.1.1. Flexure

Our investigation focuses on understanding the flexural response of the lunar lithosphere by exploring the effects of different thermal profiles, impactor sizes and varying elastic thickness values, and how large their effects are on numerical simulations from iSALE after the end of the basin formation process. The nine simulations with impactors of different size (20, 60, and 80 km) and thermal states (cold, intermediate, warm) depicted in Figure 3 serve as an are used to evaluate the accuracy and reliability of our flexure calculations (T_e = 20–100 km). The stress profiles of the numerical simulations indicate uncompensated isostatic states in the basin structures after the basin formation process. Along the radial stress profile of a given basin, certain regions exhibit subsidence (region I: basin center; region III: outer thickened part) or uplift (region II: crustal annulus) of the CrMB, which is expected, due to varying load conditions compared to the reference load, indicating potential isostatic compensation.

The flexural response of the modeled basin structures is primarily influenced by the mass excess or deficit relative to the reference model. The outer thickened parts (e.g., Figures 3b, 3d, and 3f (III)) show subsidence due to additional mass on top of the reference crust (here: T_c = 60 km), while the thickened parts near the basin center (e.g., Figures 3d, 3f, 3j, 3l, and 3p (II)) tend to experience uplift due to the absence of mass between the model surface and the reference height of 0 km, and a relatively higher proportion of crustal material than before impact. The basin center (e.g., Figures 3b, 3h, 3l, 3p, and 3r (I)), experiences subsidence due to upwelling mantle material and the need for isostatic equilibrium.

In Figures 3d, 3f, and 3j (I), the center of the basin is deeper compared to the other models shown and a depression exists at the top. The depression is not filled with crustal material during the isostatic compensation process, and this layer of void, located between the model surface and the reference surface at 0 km height, has to be considered as well.

In general, Figure 3 emphasizes the importance of mass distribution within the basin for the flexural displacements. The shape and structure of a basin following its formation are determined by both the temperature field during impact and the size of the impactor (Lompa et al., 2021a). As far as thermal profiles are concerned, the flexural displacements are more sensitive to variations in thermal profiles with larger impactors compared to smaller impactors. Flexural displacements dependent on T_e and impactor sizes are shown in Figures 3a, 3c, and 3e: In the case of a 20 km diameter impactor (Figure 3a), the flexure is influenced by T_e-values up to a maximum of 80 km, as larger T_e-values do not significantly affect flexure across all thermal profiles. For models with impactors of 60 km (Figure 3c) and 80 km (Figure 3e) in diameter, the elastic thickness can extend up to T_e = 200 km. Our results show that basins, regardless of the size of the basin, exhibit local isostasy, characterized by a low T_e. However, regional isostasy with a high T_e is observed exclusively for larger basins, showing no isostatic compensation for small basins. Consequently, for a small basin, only a very small T_e leads to a noticeable

change in *NRMSE*, limiting the explored T_e-range and having only a small T_e influence on the overall isostatic compensation process.

When a small impact crater ($L_{imp} < 30$ km) is formed on the lunar surface, the redistribution of mass caused by the excavation of the cavity is concentrated within a limited area. As a result, the flexural response of the lunar lithosphere is confined primarily to the immediate vicinity of the impact site. The localized isostatic compensation arises from the lithosphere's ability to adjust vertically to balance the loads exerted upon it within this smaller region. Flexural displacements and subsequent crustal adjustments are predominantly affected by the specific mass distribution within the basin itself. On the contrary, larger basins encompass a larger area and involve more extensive mass redistribution during their formation. Impact energy and subsequent excavation displace substantial volumes of material over a broader region. As a consequence, the isostatic response extends across a wider spatial scale, encompassing not only the basin but also its surrounding regions. This regional isostasy is manifested by flexural adjustments that spread over a larger area and reflects the need for the lithosphere to equilibrate the loads associated with the basin and its extended surroundings. It is important to note that isostasy is not always an asymptotic limit, as pointed out in the work of S. Zhong (1997) in the context of crustal compensation. Zhong's findings highlight that while the crust tends to approach an isostatic state at long wavelengths, especially beyond 800 km, crustal isostasy may not necessarily be an asymptotic limit at shorter wavelengths. This is shown with the lunar mantle uplifts we are examining, where the crust's vertical movement may not strictly follow the path toward isostatic compensation.

3.1.2. Isostatic Compensation

Our study aims at estimating the importance of isostatic adjustment processes for basins of given size using the gravity signature (Lompa et al., 2021a; Miljković et al., 2016; Wieczorek et al., 2013). To demonstrate the effect of isostasy, we show two examples in Figure 4, relating to the Orientale basin and the Landau basin, respectively. We illustrate how the position of the CrMB changes for different T_e-values and how the load distribution (Figures 4h1 and 4h2) evolves accordingly. When T_e is 0 km, the load distribution (Figures 4h1 and 4h2) is equivalent to that of the reference model (Figures 4h1 and 4h2), indicating local isostatic equilibrium. As the elastic thickness increases, the load distribution (Figures 4h1 and 4h2) approaches the load distribution without isostatic compensation (Figures 4d1 and 4d2) after impact. Consequently, the morphology of the model develops in a manner where the CrMB undergoes significant adjustments, such as uplift or subsidence, for small T_e-values, while the original state of the model is maintained for larger T_e-values. In general, models experience uplift in regions with a thickened crust (Figure 4g1 (II)). Compared to the reference model, there is an increase in less dense crustal material, resulting in the model surface being below the reference height of 0 km. The subsidence of the CrMB in the model after impact and the increased presence of low densities in the crust are compensated by uplifting this region to achieve isostatic equilibrium. The degree of uplift depends on the elastic thickness and thereby influences the local or regional isostatic effect.

Bouguer gravity signatures (Figures 4f1 and 4f2) are affected by the density contrast between the crust and the mantle, reflecting the shape of CrMB in different isostatic states. As the location of the CrMB changes, the relative positions of the masses within the isostatically compensated models also change. The shape of the Bouguer anomaly responds to both the relative density distribution within the model (density contrast between crust and mantle) and the vertical displacement of masses (subsidence or uplift). The interplay between these factors results in smaller differences in positive and negative amplitudes when the thickened crustal part moves upward. Figure 4f1 (I) shows how the signals change shapes, particularly in the transition zone between the center of the basin, dominated by the mantle material, and the adjacent crust. In this zone, the mantle and crust begin to form an anvil-like structure (Figure 4g1 (I)). The flexural response strongly affects this region, as shown by the load distribution (Figure 4h1).

The upper part of Figure 4 displays the DW-matrices for both isostatically uncompensated models (immediately after the impact; Figures 4a1 and 4a2) and isostatically compensated models (Figures 4e1 and 4e2) for different T_e-values. The ICM of the Orientale basin deviates more from the observed data (*NRMSE* ranging from 9.3 to 12.2) compared to the uncompensated model (*NRMSE* = 2.8). In this case, the chosen values for T_e do not yield an improved gravity fit after isostatic compensation. However, a better fit for the Orientale basin (*NRMSE* = 2.3) can be achieved by assuming an alternative crustal density (Table 2). For the smaller Landau basin, the best-fit is obtained when assuming an elastic thickness of 5 km (*NRMSE* = 7.4), representing an improvement over the

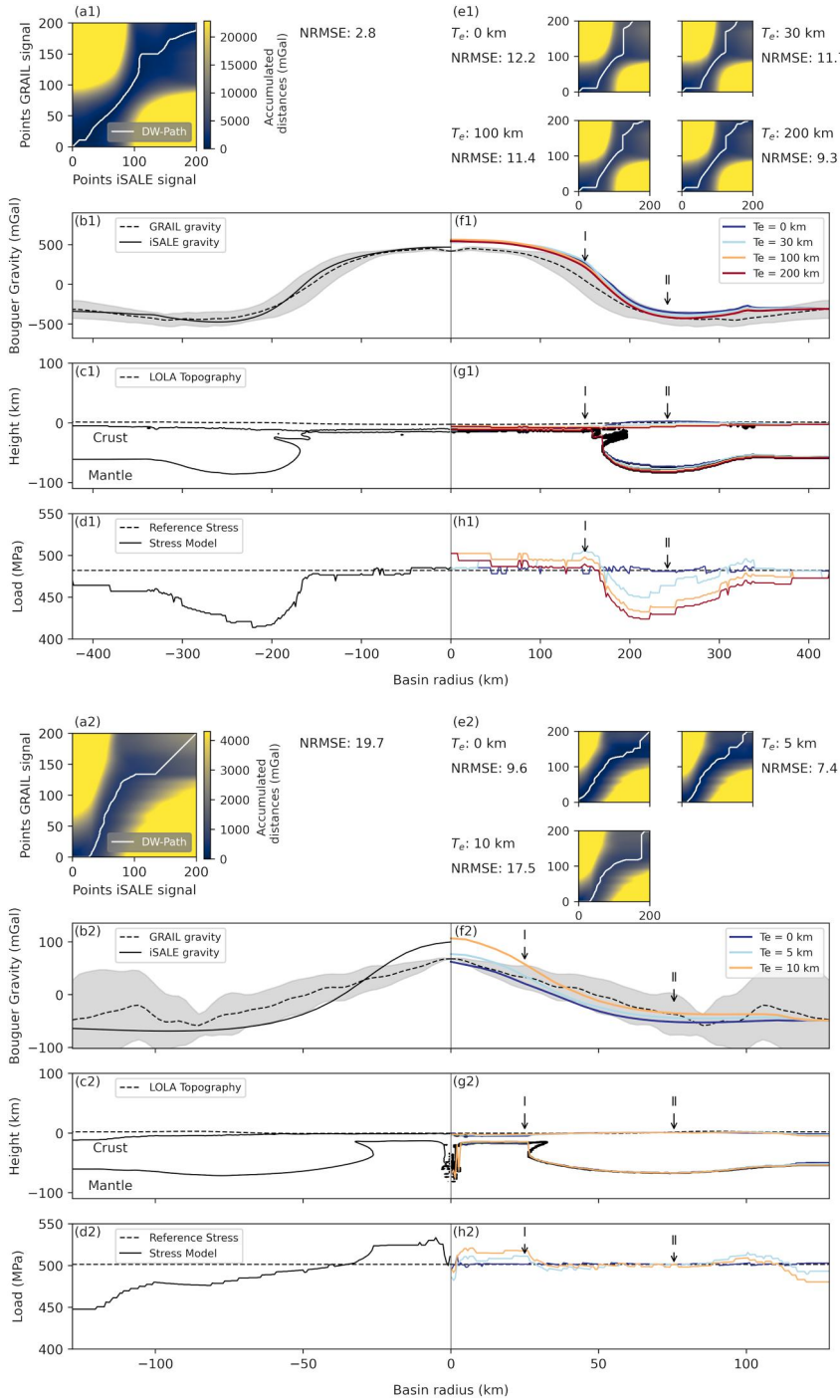

Figure 4. Section through two models of basin formation for Orientale (cold thermal profile, L_{imp} = 80 km, ρ_c = 2,750 kg m^{-3}, T_C = 60 km) (top), and Landau (intermediate thermal profile, L_{imp} = 30 km, ρ_c = 2,950 kg m^{-3}, T_C = 60 km) (bottom). The figure shows basins before (c) and after isostatic compensation (g), with its corresponding load profiles (d, h) and modeled gravity signatures (b, f). In the gravity plots (b, f), the measured gravity signature is shown with a dashed line. The colors in the gravity (f), contour (g) and load (h) plots indicate the elastic thickness value of either 0, 30, 100, or 200 km. In the load plots (d, h), the reference model is shown as a dashed line. At the top, the DW-matrices (a, e) with their deviations (*NRMSE*) are shown for isostatically uncompensated models (a) and compensated models dependent on four T_e-values (e). The numbers (I) and (II) indicate the transition zone between mantle dominated basin center, and the location, where the crust is thickest (the diameter of the largest crustal thickness (*DLCT*), compared with Lompa et al. (2021a)).

Table 2
Ages of Selected Lunar Basins and Corresponding Numerical Model Parameters

Basins		Formation time		Best-fit model parameters (Lompa et al., 2021a)				Best-fit model parameters (this study)					*NRMSE*	
ID	Name[a]	Age[b] (Ga)	Period[c]	T[d]	L_{imp} (km)	ρ_c (kg m^{-3})	T_c (km)	T	L_{imp} (km)	ρ_c (kg m^{-3})	T_c (km)	T_e (km)	Lompa et al. (2021a)	This study
1	Birkhoff	$4.29^{+0.035}_{-0.047}$	PN	W	20	2,950	40	W	20	2,850	40	0	6.5	6.1
2	Fitzgerald-Jackson	$4.26^{+0.044}_{-0.063}$	PN(*)	I	60	2,950	40	I	60	2,950	60	160	15.2	21.5
3	Dirichlet-Jackson	$4.23^{+0.022}_{-0.026}$	PN(*)	I	40	2,950	40	I	40	2,950	40	180	13.9	14.1
4	Coulomb-Sarton	$4.23^{+0.025}_{-0.030}$	PN	I	40	2,750	40	I	40	2,850	40	180	4.5	3.7
5	Fowler-Charlier	N.D.[e]	PN	I	30	2,950	40	I	30	2,950	60	120	21.4	9.0
6	Galois	N.D.	PN	I	20	2,850	60	I	20	2,850	60	80	14.1	11.6
7	Landau	N.D.	PN	I	30	2,950	60	I	30	2,950	60	5	19.7	7.4
8	Milne	N.D.	PN	I	20	2,850	40	I	30	2,650	60	0	1.2	1.8
9	Mendeleev	$4.13^{+0.044}_{-0.064}$	N; N/PN(*)	I	50	2,950	60	I	50	2,950	60	180	18.9	21.0
10	Korolev	$4.11^{+0.021}_{-0.025}$	N; N/PN(*)	I	50	2,950	60	I	50	2,950	60	180	23.8	28.5
11	Hertzsprung	$4.09^{+0.030}_{-0.027}$	N; N/PN(*)	I	60	2,950	60	I	60	2,950	60	180	5.3	5.1
12	Orientale	$3.81^{+0.0081}_{-0.0085}$	LI	C	80	2,750	60	C	80	2,850	60	140	2.8	2.3
13	D'Alembert	N.D.	N.D.	I	20	2,750	60	I	20	2,850	60	80	5.1	9.6
14	Harkhebi	N.D.	N.D.	I	30	2,950	60	C	20	2,950	60	20	13.0	7.8
15	Poczobutt	N.D.	N.D.	W	20	2,950	40	C	20	2,750	60	80	17.6	4.8
16	TOPO-22	N.D.	N.D.	W	40	2,950	40	I	40	2,950	60	180	5.1	1.5

[a]Basin nomenclatures are approved by the International Astronomical Union (IAU) or suggested by Neumann et al. (2015). [b]From Orgel et al. (2018, Table 2). [c]Periods from Wilhelms et al. (1987); if indicated with (*) periods taken from Fassett et al. (2012). [d]W = Warm (Ages ca. 4.4 Ga), I = Intermediate (Ages ca. 4.1 Ga), C = Cold (Ages ca. 3.8 Ga). [e]N.D.: Not determined.

uncompensated model (*NRMSE* = 19.7). It is important to note that our analysis is constrained by a database of only 16 basins, limiting its scope. Most basins show best fits with intermediate thermal profiles, possibly affecting the accurate representation of warm profile elastic thickness. The warm scenario may experience significant impact heating, altering post-impact thermal structure and reducing effective elastic thickness. In contrast, the impact heating effect is less pronounced in the cold scenario, resulting in a comparatively minor difference in the cold case situation (see Appendix A).

3.2. Process-Oriented Gravity Modeling of Lunar Farside Basins

We performed process-oriented gravity modeling for 16 lunar farside basins (Lompa et al., 2021a). Our aim is to determine the best-fit model for each basin by minimizing the *NRMSE* value of the DW-matrices. Additionally, we use the age of the basins, based on crater counting (Orgel et al., 2018), as a further constraint for the thermal state of the crust. From the modeling process, we obtain the thickness of the elastic lithosphere, providing insight into the isostatic state of the basins. Furthermore, we examined whether the impactor size, thermal state, crustal density, and crustal thickness of the best-fit models differ from the findings in Lompa et al. (2021a).

3.2.1. Elastic Thickness

To investigate the effects of isostatic compensation on choice of the best-fit model, we use T_e as a free parameter for isostatically compensated models (referred to as "T_e local" in the figures). For comparison, we include the results of the isostatically uncompensated models of Lompa et al. (2021a) in Table 2. The table presents the set of best-fit model parameters, including impactor diameter (L_{imp}), crustal thickness (T_c) and density (ρ_c), thermal profile (T), elastic thickness value (T_e), and the corresponding values of *NRMSE*. For further reference, we provide comparisons between the previous (uncompensated) and new (compensated) best-fit models, along with structure models, gravity signatures, and DW-matrices in Supporting Information S1 (Figures S1–S16 in Supporting Information S1).

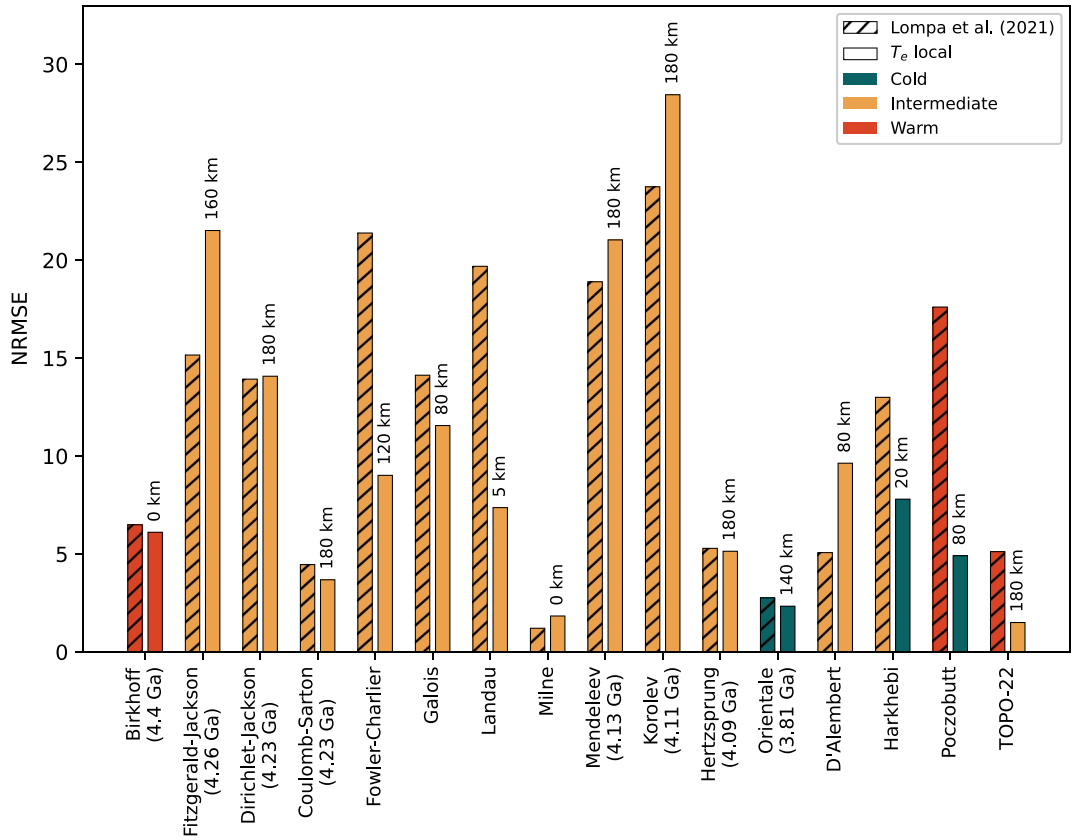

Figure 5. Comparison of *NRMSE*-values for the best-fit models of the lunar farside basins, represented by hatched bars (isostatically uncompensated models from Lompa et al. (2021a)) and non-hatched bars (isostatically compensated models). The models consider different thermal conditions (blue: cold; yellow: intermediate; orange: warm) and are annotated with the corresponding elastic thickness assumptions.

To demonstrate the effects, Figure 5 illustrates the *NRMSE*-values in relation to both the previous uncompensated best-fit models from Lompa et al. (2021a) and the isostatically compensated best-fit models. First, we observe that the choice of the assumed thermal profile used in the basin formation models remains unchanged when considering isostatic compensation, except for three basins (Harkhebi, Poczobutt, TOPO-22). It is essential to note that precise age data for these structures are lacking (Table 2) and, therefore, the thermal profile at the time of impact is not constrained.

Based on the change in *NRMSE* ($\Delta NRMSE$) between the isostatically compensated and uncompensated models, we categorize the fits into three groups. This assessment was made after visually comparing the gravity signatures. The visual comparisons can be found in Supporting Information S1 (Figures S1–S16 in Supporting Information S1):

- A change in *NRMSE* of smaller than -3 indicates a significant improvement in the best-fit models.
- A change greater than $+3$ suggests that isostatic compensation did not lead to improvements.
- Values between -3 and $+3$ indicate that fits are not significantly affected by isostatic compensation.

3.2.2. Effect of the Thermal State

To investigate the relationship between the elastic thickness and the thermal state of the Moon, we conducted an analysis to determine the average elastic thickness for three different thermal profiles. We assume that the elastic thickness increases as the targets transition from warm to cold. This assumption is justified by the lower rigidity (D) and smaller elastic thickness in warm targets, while the opposite is true for cold targets.

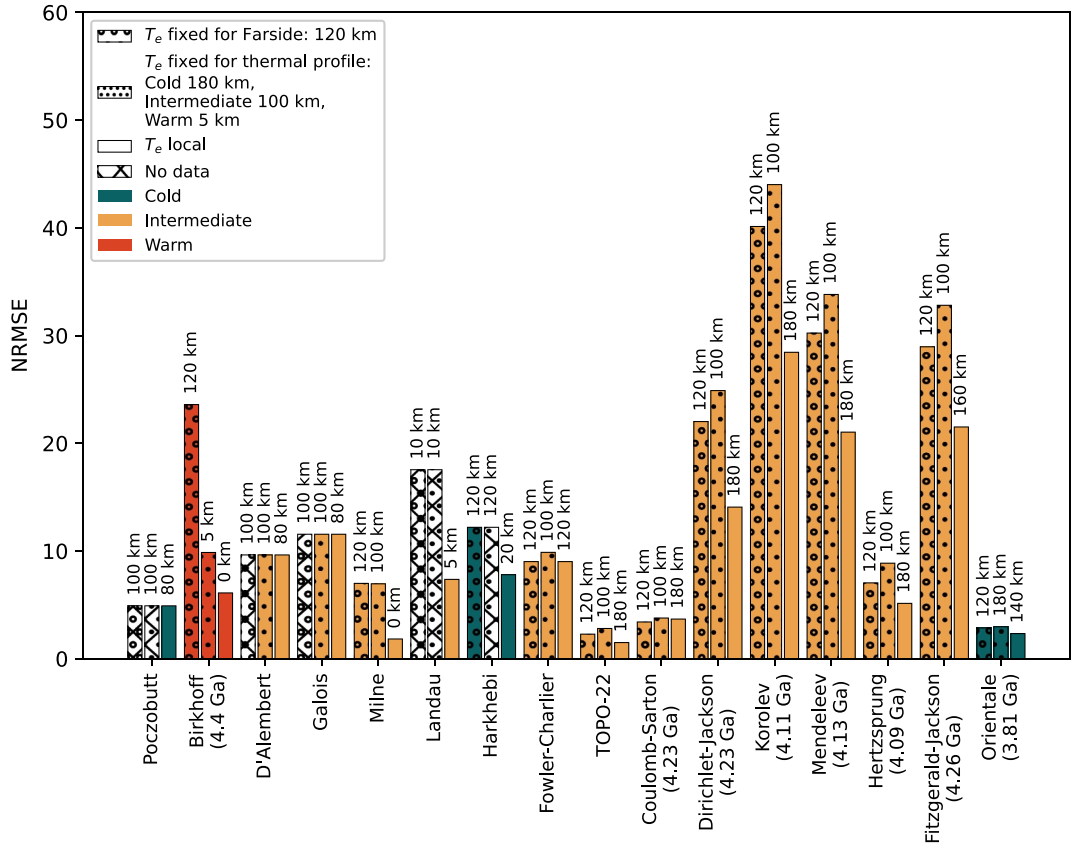

Figure 6. *NRMSE*-values for best-fit models, showcasing mean elastic thickness for the farside (bars with circles), elastic thickness variations based on thermal profiles (bars with dots), and best-fit models assuming basin-specific elastic thickness (no hatched bars) across 16 lunar farside basins. The color-coded bars correspond to distinct thermal conditions employed in the models (blue: cold; yellow: intermediate; orange: warm). Unfilled bars indicate models lacking data for the assumed elastic thickness, for which the subsequent available T_e and corresponding *NRMSE*-values were considered. The associated T_e-values are labeled adjacent to the respective bars. Basin arrangement is in ascending order of basin size.

To obtain temperature-dependent elastic thickness values, we used our POGM, considering the T_e-range from 0 to 200 km. Independently of the individual basin fitting, we selected the T_e-value with the smallest *NRMSE*-value for each basin and thermal profile. As a result, we determined mean elastic thicknesses of 5, 100, and 180 km for warm, intermediate, and cold targets, respectively.

The increase in elastic thicknesses from warm to cold targets corresponds to the assumption that a warm target has a low rigidity and thus a small T_e, and for cold targets vice versa. For the lunar farside, we found a mean elastic thickness of 120 km.

Figure 6 depicts the *NRMSE*-values for each basin under different assumptions. The basins are sorted in ascending order based on size, while the colors of the bars indicate the thermal profile used in the best-fit model, and the accompanying numbers represent the corresponding *NRMSE*-values. When assuming average T_e-values for each thermal profile (bars with filled dots), the deviations tend to be larger than for a mean T_e for the entire farside (bars with circles). However, the Birkhoff crater presents an exception to this trend, as the farside T_e yields a poorer fit than the mean thermal T_e. In all cases, the *NRMSE* is minimized when an individual elastic thickness is assumed for each basin.

Uncolored bars indicate instances where no models are available because the algorithm stopped iterating over T_e due to the lack of significant gravity changes compared to the previously used T_e-value. Nevertheless, we provide *NRMSE*-values next to these bars to represent the next potential deviation value in the dataset. It is important to note that the *NRMSE*-values remain constant indicating that small basins cannot effectively constrain large elastic

thicknesses. In addition, the T_e-values should be considered as a minimum elastic thickness and do not represent exact values.

4. Discussion

4.1. Variations of the Elastic Thickness

4.1.1. Location

The results of our study show varying elastic thicknesses in different basins on the lunar farside. To put our data into a global spatial context, we plotted our elastic thickness data on a crustal thickness map derived from global gravity data (Wieczorek et al., 2013) (Figure 7a). We see that large elastic thicknesses correspond to regions with large crustal thicknesses, and vice versa.

We used the FeO abundance determined from the Lunar Prospector gamma ray spectroscopy data (Prettyman et al., 2006) (Figure 7b) to get deeper insights into the geochemical composition of the areas where the basins are located. In general, all investigated basins are located within the Feldspathic Highlands Terrane (FHT) (Jolliff et al., 2000), which is characterized by a highly elevated topographic region and an anorthositic composition, rich in plagioclase feldspar (Jolliff et al., 2000). Based on its geochemistry, the FHT can be divided into two areas: (a) a central highly anorthositic region (FHT-An), depleted in FeO (FeO < 5 weight %; blue colors in Figure 7b) and Th, corresponding to the thickest part of the crust (Figure 7a), and (b) an outer FHT region (FHT-O) corresponding to all surface areas outside the boundaries of FHT-An, mare-infills, PKT or SPA (Jolliff et al., 2000). 14 of our 16 studied basins are placed in the FHT-An region (Figure 7b, blue colors). Milne (No. 8) and Harkhebi (No. 14) are located in the FHT-O region (Figure 7b, brownish colors). Our results show that the elastic thicknesses of our studied basins are large (80 km < T_e < 180 km) in the FHT-An region, which correlates with the expected large crustal thickness in this area (Figure 7a). In the transition and inside the FHT-O region both the elastic thickness (e.g., Audet, 2014) and the crustal thickness becomes thinner, which corresponds to our modeling results for the basins Milne and Harkhebi located in this area (Figures 7a and 7b).

The trend we see in the modeled elastic thicknesses can be reconciled with the proposed formation history of the lunar highlands: The FHT is thought to be the most ancient terrane on the Moon (e.g., Elkins-Tanton et al., 2011; Jolliff et al., 2000), formed as a result of the cooling and solidification of the magma ocean and the associated floating of plagioclase feldspar eventually lead to the formation of a thick anorthosite crust (e.g., Elkins-Tanton et al., 2011; Warren, 1985). Due to this early differentiation, the thicker crust and higher elastic thicknesses—compared to the SPA, FHT-O, and Mare regions—of the central FHT may be due to the stronger lithospheric support provided by a more rigid and cooler lithosphere. Kamata et al. (2013) show that the central FHT requires a cold interior. Therefore, the thermal field is characterized by lower surface temperatures in areas with thicker crust and higher elastic thickness, and thus less isostatic adjustment compared to the lunar Maria. This may be attributed to the greater insulation provided by the thicker crust, which slows the transfer of heat from the interior to the surface.

4.1.2. Time

To analyze the variations of the elastic thickness with time, we consider the cooling history of the Moon. For this, we plot the elastic thickness from our basin formation models as a function of time (Figure 8). The x-axis represents time starting from the formation of the Moon (ca. 4.4 Ga ago) until the end of the basin formation period, ca. 3.8 Ga ago. The basins with age estimates from crater counting (Table 2) are displayed at their respective formation time. Basins without precise dating information are plotted at the ages associated with their assumed temperature profiles (3.8, 4.1, and 4.4 Ga), based on the best fit between observed gravity and our models.

Our results show that 12 of the 16 basins on the farside formed within a relatively short duration of 200 million years, between 4.3 and 4.1 Ga (orange circles) (Figure 8). Specifically, seven of these basins exhibit an elastic thickness greater than 150 km (No. 2, 3, 4, 9, 10, 11, 16), indicating a significant variation in mechanical properties. Elastic thickness greater than 150 km indicates a thicker and stronger lithosphere in those locations. All of these basins are located within the FHT-An region, while three basins (No. 3, 10, 11) are located within the thickest crustal area (T_c > 60 km) (Figure 7a). The remaining basins (No. 3, 4, 9, 16) are located in regions with crustal thicknesses of approximately 40–50 km (Figure 7a).

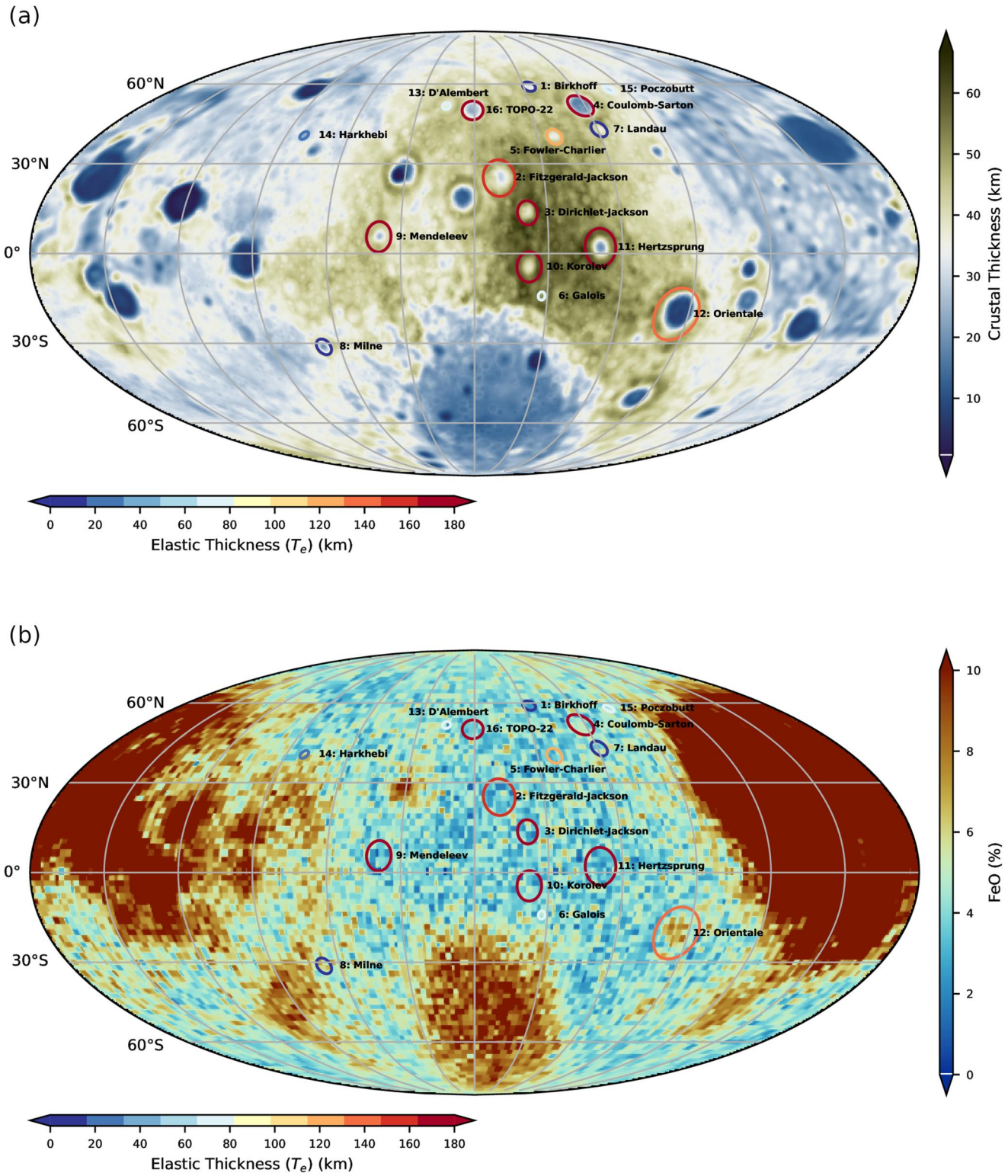
(a)
60°N
30°N
0°
30°S
60°S
13: D'Alembert
1: Birkhoff
15: Poczobutt
16: TOPO-22
4: Coulomb-Sarton
7: Landau
14: Harkhebi
5: Fowler-Charlier
2: Fitzgerald-Jackson
3: Dirichlet-Jackson
9: Mendeleev
11: Hertzsprung
10: Korolev
6: Galois
12: Orientale
8: Milne
Crustal Thickness (km)
10
20
30
40
50
60
0
20
40
60
80
100
120
140
160
180
Elastic Thickness (T_e) (km)
(b)
60°N
30°N
0°
30°S
60°S
13: D'Alembert
1: Birkhoff
15: Poczobutt
16: TOPO-22
4: Coulomb-Sarton
7: Landau
14: Harkhebi
5: Fowler-Charlier
2: Fitzgerald-Jackson
3: Dirichlet-Jackson
9: Mendeleev
11: Hertzsprung
10: Korolev
6: Galois
12: Orientale
8: Milne
FeO (%)
0
2
4
6
8
10
0
20
40
60
80
100
120
140
160
180
Elastic Thickness (T_e) (km)

Figure 7.

Regardless of the age, nine investigated basins have elastic thicknesses smaller than 150 km (No. 1, 5, 6, 7, 8, 12, 13, 14, 15). This observation suggests the presence of regions with a weaker subsurface structure, indicated by a thinner and less competent lithosphere.

These findings emphasize the complex and diverse nature of the lunar farside basins, indicating that their mechanical properties are not solely controlled by the age of the basin. The presence of basins with larger and smaller elastic thickness values suggests that multiple factors played a role in shaping subsurface structures and their subsequent evolution, such as variations in composition, thermal cooling history, and the intensity of subsequent bombardment.

4.1.3. Impactor Sizes

Our investigation of the isostatic analysis of the formation models of 16 impact structures reveals a striking trend: the elastic thickness shows a clear correlation with the impactor size, as illustrated in the best-fit models in Table 2. Figure 8 shows this correlation, depicting a distinct pattern of small elastic thicknesses corresponding to small impactors (depicted by the size of the circles) and, conversely, larger elastic thicknesses aligned with larger impactors.

Interestingly, our findings suggest that, for smaller basins, flexural displacements remain constant or reach an indistinguishable state for T_e-values that exceed a critical threshold. This implies that our determined T_e-values represent rather minimum values than the exact elastic thicknesses. Furthermore, it is crucial to note that we have presented a single best-fit value, which could be potentially misleading.

4.2. Limitations of the Lithospheric Flexure Model

4.2.1. Thermal Cooling

To investigate the long-term evolution of gravity signatures in lunar impact basins, some simplifications had to be made. One of these is how we account for contraction as a consequence of cooling of thermally expanded material due to impact-induced heating and melting. We approximate the effect following our previous study (Lompa et al., 2021a) by assuming that after cooling the densities correspond to the pre-impact initial densities of the crust and mantle, which may be considered as the "cold density" of the respective lithology. However, the long-term cooling, which resulted in a gradual contraction of matter and an increase in density compared to the thermally expanded state immediately after impact, may have caused additional material motion, such as down-welling of the basin floor. The distinction of such processes from isostatic adjustment is challenging. Previous studies that employed FE modeling to account for dynamic, time-dependent processes (Ding & Zhu, 2022; Freed et al., 2014; Melosh et al., 2013) do not distinguish between contributions from pure isostasy as a consequence of static density differences between mantle and crust material and changes in density as a result of contraction from thermal cooling. The effects of thermal cooling is implicitly considered in FE modeling as density changes of impact heated materials, which is a more realistic representation. In our approach, mass is not conserved in a strict sense, which is why mass excesses tend to be overestimated and contraction-induced down-welling is underestimated. Despite these simplifications our findings align with the results for the lunar farside basins from Ding and Zhu (2022) with respect to the occurrence of exclusively vertical compensatory movements (Figure 6, therein), and that farside structures—namely Fitzgerald-Jackson, Dirichlet-Jackson, Coulomb-Sarton and TOPO-22 (Figure 7, therein)—are classified as partially relaxed structures or not relaxed structures which is in agreement with the exhibited high T_e-values in our analysis, suggesting no compensation or a regional isostatic compensation.

Figure 7. (a) Crustal thickness map of the Moon (crustal thickness model No. 1 from Wieczorek et al. (2013)) in Mollweide projection centered on the farside at 180° longitude, created with SHTools (Wieczorek & Meschede, 2018; Wieczorek et al., 2022). The investigated basins are marked by circles. The colors of the circles highlight the elastic thickness of the individual basins (blue: small T_e; red: high T_e), the size of the circles represent the basin sizes. (b) Map of FeO abundance (weight %) acquired by the Lunar Prospector and processed in 2-degree equal-area tiles (Prettyman et al., 2006). To highlight the Feldspathic Highlands Terrane areas in blue show FeO content less than 5 weight % (representing FHT-An; Jolliff et al., 2000), whereas brown areas show more than 5 weight % FeO (representing FHT-O, PKT, SPA, mare infills; Jolliff et al., 2000).

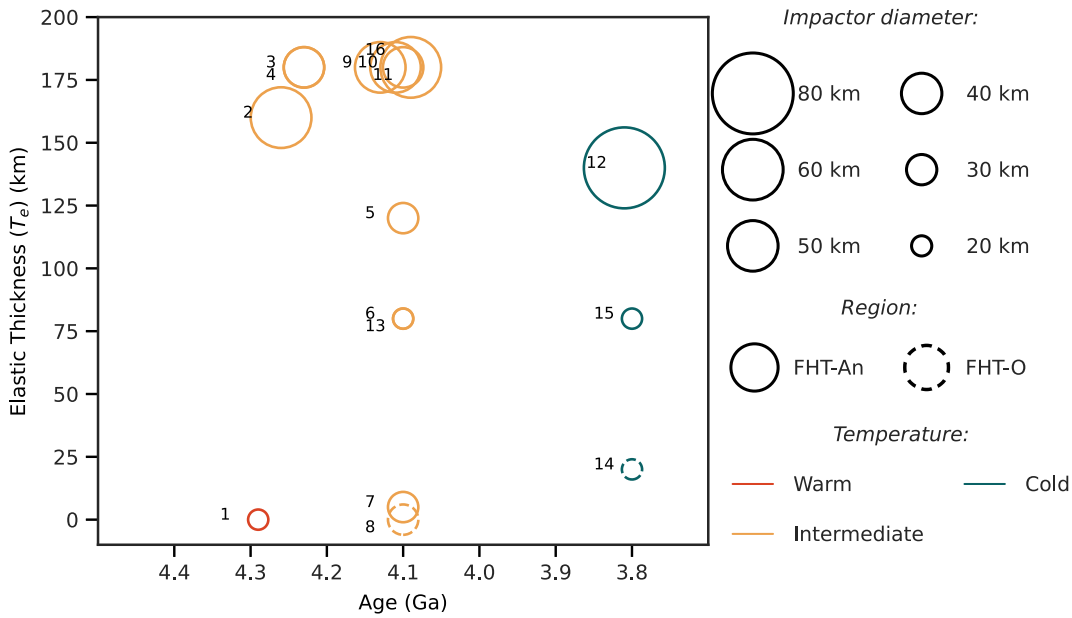

Figure 8. T_e as a function of time. The lower x-axis shows the ages related to the thermal evolution model. Colors of the circles indicate the used thermal profile, dashed/solid line styles indicate the region where the basin is located (FHT-An or FHT-O), the size of the circles represent the size of impactor in the numerical best-fit models. The numbering is related to the ID's of the 16 basins, as listed in Table 2. Example: The basin with the number 12 is the Orientale basin, which has formed in the outer FHT region in a cold target by an impactor of 80 km in size and 3.82 Ga ago. T_e for Orientale is 140 km.

4.2.2. Uniform Elastic Thickness in Impact Basins

In our study, we used a lithospheric flexure model featuring uniform elastic thicknesses throughout the impact structures. Figure 4 shows the center of the basin (I) and the transition zone (II), characterized by the thickest crust. In particular, the basin center experienced significant heating during the impact event, suggesting an anticipated preference for smaller T_e-values compared to the outer regions.

As our study advances, we recognize the need for a more refined modeling approach. Specifically, future research should explore the implementation of a variable T_e model to capture spatial complexities and refine the accuracy of our basin simulations.

4.3. Comparison to Previous Studies

In our study, we used a lithospheric flexure model to investigate the post-impact relaxation process in different sized lunar basins. The farside is characterized by its relatively thick crust, and our study primarily examines impact basins located within the anorthositic farside highlands region (FHT-An). Moreover, the lunar farside is relatively cold compared to the near side and the KREEP terrane.

4.3.1. Topographic Loading

We analyze the flexure profiles of the lunar crust based on comprehensive loads from both crustal and mantle materials, extending up to a reference depth of 100 km (Figure 3) from our numerical models. Throughout our simulations, we consistently observe a strong correlation between lunar topography and crustal flexure. Positive topographic features, such as mountains or highlands, exhibit negative flexure, while negative topography, such as basins and mare plains, corresponds to positive flexure. This clear relationship emphasizes the significant role of topographic loading in the achievement of isostatic equilibrium in our models. This outcome is in agreement with the study of Audet (2014) who shows that the load on the lunar farside is caused by topographic loading, while the near side is characterized by subsurface loading.

4.3.2. Initial Thermal State

Insights into the relationship between the initial thermal state and the deformation of the lunar lithosphere are given by Kamata et al. (2013). They emphasize that the initial thermal state strongly controls the CrMB signature, which represents the ratio of the final uplift of the mantle to the initial uplift, quantifying the level of deformation. Maintaining mantle uplifts with a 70 km crust requires an initial surface temperature gradient of less than 20 K/km. Additionally, they found that initial Moho temperatures of less than approximately 1,200 K are required to maintain mantle uplifts under all crustal thickness conditions.

Considering the information from Kamata et al. (2013) and the characteristics of our study area, it is likely that the lithospheric flexure model, assuming elastic behavior, can be successfully applied to the lunar farside with its relatively cold thermal profiles and thick crust. The temperature gradients in our study fall within the temperature limits necessary to maintain mantle uplifts, which justifies that our models can provide insights into the bending and deformation of the lunar lithosphere.

The range of thermal profiles is also in agreement with the study of Ding and Zhu (2022) where a near-surface temperature gradient less than 20 and 10 K/km for the lunar farside is assumed (Appendix A, Figure A1). The thermal profiles outlined in our study and the work of Ding and Zhu (2022) play a crucial role in the determination of material properties, including viscous parameters, in the modeling. Elevated temperatures and Thorium content, as assumed for the lunar near side and the KREEP terrane in Ding and Zhu (2022), influence the viscous behavior of material flow over time. In our study, the thermal profiles are such that the consideration of viscous behavior, typically explicitly addressed in FE modeling, becomes negligible in our lithospheric flexure modeling. It is important to note that the elastic-shell model that we use does not simulate an instantaneous response, despite its "elastic" designation. With the exception of a liquid layer, the solid layer behaves as an elastic body, instantaneously. This implies that the elastic thickness is equal to the sum of the crust and the thickness of the entire mantle. However, for a long-term limit, the use of an elastic-shell model becomes appropriate because of the pronounced dependence of viscosity on temperature. In this context, our modeling approach accommodates the temporal complexities of the lithospheric response, offering a comprehensive representation of the lunar lithosphere under varying thermal conditions.

4.3.3. Variations in Elastic Thickness

In our study, we tested both a fixed, time-independent elastic thickness of 120 km for the lunar farside and three time-dependent elastic thicknesses related to the formation time of a basin (5 km for warm conditions, 100 km for intermediate conditions, and 180 km for cold conditions) as minimum values for each basin. Our findings demonstrate that the use of a basin-specific elastic thickness leads to a smaller *NRMSE*-value compared to a constant T_e for the lunar farside or a T_e dependent on the thermal profile. Nevertheless, using a varying elastic thickness for individual basins yields the best agreement between observed gravity signatures and isostatically compensated gravity data from basin formation models. These findings suggest that the elastic thickness is not constant for the whole Moon and that the cooling history and thermal state at the time of impact differ among the basins, resulting in variations in their mechanical properties.

The finding of varying elastic thicknesses on the lunar surface aligns with studies by Huang and Wieczorek (2012), Z. Zhong, Yan, Alexis, and Rodriguez (2019), Z. Zhong, Yan, Zhang, et al. (2019), and Z. Zhong et al. (2018). They investigated the size of the elastic thickness for different locations on the Moon (Figure 1, triangles left and right) using the admittance method. Their T_e-values range from 5 to 30 km and from 0 to 150 km which fits to our modeled T_e-values. Deviations in T_e-values likely originate from different methodological approaches. In the studies mentioned above, the admittance method was used, in which spatial variations in topography and gravity anomalies and were analyzed and compared with the expected response of the elastic plate. On the other hand, process-oriented gravity modeling using a flexure model takes a more comprehensive approach to estimate the elastic thickness. It is important to note that although the admittance method incorporates a lithospheric flexure, it usually assumes a simplified, unrealistic loading for impact basins, such as fully uncorrelated surface and sub-surface loading. In contrast, our study uses the output of iSALE simulations, which allows for considering a realistic loading pattern. This approach takes into account variations in lithospheric strength, lateral heterogeneity and the presence of density anomalies, all of which affect estimates of elastic thickness. The addition of these complexities provides an improved representation of the lithosphere's flexural response.

5. Conclusion

Our investigation of lunar basin formation involves the analysis of long-term isostatic adjustments of formation models, which are constrained by gravity data. This analysis offers valuable insights into estimating the sizes of impactors that formed the basins. Although determining the actual size of a basin is challenging due to non-pristine topographic expressions, gravity data prove to be a reliable constraint that is less affected by alteration processes.

Lompa et al. (2021a) explored various thermal states, impactor sizes, and crustal thicknesses, establishing a direct relationship between the present-day gravity signatures and impactor sizes for 16 selected lunar farside basins. Our study indicates that isostasy causes minor changes in the amplitude of the basin's gravity signature, while the width and position of the maximum and minimum remain relatively stable. Consequently, previously suggested estimates of basin size, derived from gravity anomaly, and the sizes of impactors that form specific basins, are only slightly affected.

In general, variations in elastic thickness across the lunar farside underscores the complexity of impact basins, emphasizing the necessity for a comprehensive understanding of their formation and evolution. Our study shows that the knowledge about elastic thickness does not influence the estimation of impactor size.

Appendix A: Elastic Thickness Derived From Thermal Profiles

In the process-oriented gravity modeling process, the elastic thickness is considered as a free parameter determined by model fitting. However, the elastic thickness depends on the thermal structure and can thus be estimated from the rheological properties of the crust and the mantle.

To assess the degree to which the elastic thickness depends on the thermal profiles used, we compare our model temperatures, viscosities and elastic thicknesses with those of Ding and Zhu (2022). First, we calculate the viscosity (η) as a function of the temperature from the thermal profiles we assume for different basin formation ages (warm, intermediate, cold; Figure A1a). In a second step, we estimate the rigidity (μ) from the elastic parameters. The Maxwell time (τ_M), which defines the time scale when viscous behavior transitions into elastic relaxation processes, is then given by the ratio of viscosity and rigidity

$$\tau_M \equiv \frac{\eta}{\mu} \tag{A1}$$

with the rigidity

$$\mu = \frac{E}{2(1+\nu)} \tag{A2}$$

where E corresponds to Young's modulus and ν is the Poisson ratio (see Table 1). The region in which the Maxwell time exceeds the timescale that corresponds to one of the three thermal profiles, the assumption of elastic behavior of the lithosphere is justified (e.g., Melosh, 2011).

According to the approach outlined by Ding and Zhu (2022) and Kamata et al. (2015), we employ temperature-dependent viscosity values of dry anorthite (Rybacki & Dresen, 2000) for the crust and values of dry peridotite (Lawlis, 1998) for the mantle. We use the equation

$$\eta = \frac{1}{2A}\sigma^{(1-n)}e^{\frac{E^*}{RT}} \tag{A3}$$

with the pre-exponential factor A, stress exponent n, activation energy E^*, and gas constant R (Table A1).

The temperature T as a function of depth is the key. We set a reference stress level σ of 30 MPa. Additionally, we ensure that the viscosity falls within the range of 10^{19}–10^{30} Pa · s, following the approaches taken by Ding and Zhu (2022), Freed et al. (2014), and Kamata et al. (2015).

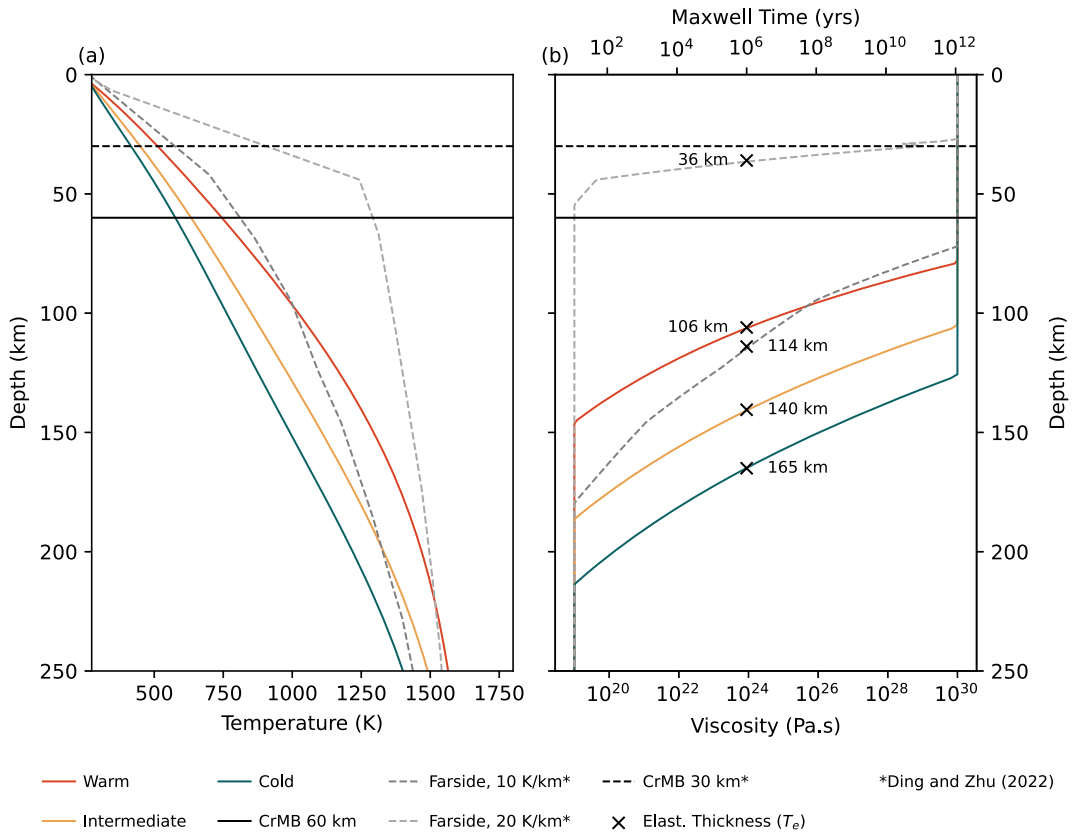

Figure A1. Temperature (a) and viscosity and Maxwell time (b) profiles as a function of depth for three different thermal states of the lunar farside. The horizontal solid and dashed lines mark the crust-mantle boundaries (CrMB) in 30 and 60 km depth, respectively. (a) Temperature profiles are based on thermal evolution models (blue, cold; yellow, intermediate; orange, warm) used in combination with a CrMB in 60 km depth. Dashed lines (farside, 10 and 20 K/km, CrMB = 30 km) show the temperature profiles and CrMB used in the work of Ding and Zhu (2022). (b) Viscosity and Maxwell time profiles for all thermal profiles refer to a 60 km (colored solid lines) and 30 km thick crust (gray dashed lines) (Ding & Zhu, 2022). Crosses indicate elastic thicknesses (T_e) for a Maxwell time of 1 million (10^6) years.

In Figure A1a, we present thermal profiles as functions of depth, used in our numerical simulations to represent distinct thermal states on the lunar farside, namely cold (blue), intermediate (yellow) and warm (orange) conditions (see also Lompa et al. (2021a); Figure 1). Furthermore, we show the resulting viscosity profiles (Equation A3) and Maxwell times (Equation A1) as functions of depth (Figure A1b). Maxwell times represent the characteristic timescales for the material to respond to the applied stress. For example, if we assume a Maxwell time of 1 million years (10^6 years), this corresponds to the time it takes for the material to deform plastically under the given load. The thicknesses of the lithosphere—about 106 km for the warm state, 140 km for the intermediate state and 165 km for the cold state (Figure A1b)—depend on the prevailing thermal conditions on the farside of the Moon. For comparison, the elastic thicknesses determined through a POGM (Section 3.2.2) are 180 km (cold), 100 km (intermediate) and 5 km (warm). The elastic thicknesses of the two different approaches (estimated values directly calculated from the temperature profiles and the results from the process-oriented gravity modeling) align well except for the warm temperature profile (106 vs. 5 km). It is important to note that our database comprises only 16 basins, which limits the extent of our analysis. For most basins from the dataset, the best-fits for the numerical models have been found for the intermediate thermal profiles. Consequently, there is a possibility that our analysis may not accurately represent the elastic thickness of the warm profile. Another plausible explanation is that, in the warm case, impact heating substantially alters the post-impact thermal structure, leading to a reduction in the effective elastic

Table A1
Material Parameters to Determine Viscosity Profiles in Crust and Mantle

Symbol	Parameter	Crustal value	Mantle value
A	Pre-exponential factor	$10^{12.7}$ MPa^{-n} s^{-1}	$10^{7.6}$ MPa^{-n} s^{-1}
E^*	Activation energy	648 kJ mol^{-1}	600 kJ mol^{-1}
n	Stress component	3	3.5
R	Gas constant	8.31 J mol^{-1} K^{-1}	
T	Temperature	Value of the temperature profile dependent on depth (in K)	

thickness. In contrast, the impact heating effect is less pronounced for the cold case, resulting in a comparatively less notable difference in the cold case scenario.

For comparison, we calculated Maxwell time profiles (Figure A1b, dashed lines) using the 10 and 20 K/km temperature profiles (Figure A1a, dashed lines) and the corresponding viscosity data (Figure A1b, dashed lines) from Ding and Zhu (2022) (Figures 3b and 3c therein) which are representative for the lunar farside. Figure A1b shows that the elastic thicknesses are between 36 km (20 K/km) and 114 km (10 K/km) for a Maxwell time of 1 million years. The profiles of Ding and Zhu (2022) are warmer and, therefore, the calculated elastic thicknesses are smaller.

Data Availability Statement

We used the iSALE shock-physics hydrocode ("Dellen") for numerical modeling in this work. The stable release is available at https://isale-code.github.io/. Information about and data for numerical models are available in Lompa et al. (2021a) and the corresponding repository Lompa et al. (2021b). The data from this study are stored in the repository Lompa et al. (2023): When downloading the zip-archive, you get a Python package with all code snippets, data for the best-fit models, and the data you need to reproduce all figures. In the Python package, the iSALE models can be accessed without having iSALE installed. Data for crustal thickness maps are available in the repository Wieczorek (2012). Data for the 2-degree FeO abundance map can be accessed via NASA PDS (Planetary Data System) with the "Lunar Orbital Data Explorer" and then Lunar Prospector—GRS Gamma Ray Spectrometer—Derived Data—Gamma Ray Spectra Elemental Abundance Product (DERABU) (ode.rsl.wustl.edu/moon/productsearch). These datasets are also available in the repository Lompa et al. (2023).

Acknowledgments
We sincerely thank Dr. Nils Holzrichter from Kiel University for contributing to this article. The authors thank the developers of iSALE-2D and the pySALEPlot tool for the numerical modeling. The authors thank the developers of GMT (Wessel et al., 2019), Cartopy (Elson et al., 2021), and SHTools (Wieczorek & Meschede, 2018; Wieczorek et al., 2022) for their unrestricted access and free use of their tools. This work was funded by the Deutsche Forschungsgemeinschaft in the project 263649064 TRR-170. The authors thank the associated editor Katarina Miljković, and Min Ding and an anonymous reviewer for their helpful comments to improve the manuscript. Open Access funding enabled and organized by Projekt DEAL.

References

Audet, P. (2014). Toward mapping the effective elastic thickness of planetary lithospheres from a spherical wavelet analysis of gravity and topography. *Physics of the Earth and Planetary Interiors*, *226*, 48–82. https://doi.org/10.1016/j.pepi.2013.09.011

Burov, E. B., & Diament, M. (1995). The effective elastic thickness (T_e) of continental lithosphere: What does it really mean? *Journal of Geophysical Research*, *100*(B3), 3905–3927. https://doi.org/10.1029/94JB02770

Collins, G. S. (2014). Numerical simulations of impact crater formation with dilatancy. *Journal of Geophysical Research: Planets*, *119*(12), 2600–2619. https://doi.org/10.1002/2014je004708

Conrad, J. W., Nimmo, F., Fassett, C. I., & Kamata, S. (2018). Lunar impact history constrained by GRAIL-derived basin relaxation measurements. *Icarus*, *314*, 50–63. https://doi.org/10.1016/j.icarus.2018.05.029

Crosby, A., & McKenzie, D. (2005). Measurements of the elastic thickness under ancient lunar terrain. *Icarus*, *173*(1), 100–107. https://doi.org/10.1016/j.icarus.2004.07.017

Ding, M., & Zhu, M.-H. (2022). Effects of regional thermal state on the crustal annulus relaxation of lunar large impact basins. *Journal of Geophysical Research: Planets*, *127*(3), e2021JE007132. https://doi.org/10.1029/2021je007132

Elkins-Tanton, L. T., Burgess, S., & Yin, Q.-Z. (2011). The lunar magma ocean: Reconciling the solidification process with lunar petrology and geochronology. *Earth and Planetary Science Letters*, *304*(3–4), 326–336. https://doi.org/10.1016/j.epsl.2011.02.004

Elson, P., de Andrade, E. S., Hattersley, R., May, R., Lucas, G., Campbell, E., et al. (2021). Scitools/cartopy: v0.19.0.post1. *Zenodo*. https://doi.org/10.5281/zenodo.4716221

Fassett, C. I., Head, J. W., Kadish, S. J., Mazarico, E., Neumann, G. A., Smith, D. E., & Zuber, M. T. (2012). Lunar impact basins: Stratigraphy, sequence and ages from superposed impact crater populations measured from lunar orbiter laser altimeter (LOLA) data. *Journal of Geophysical Research*, *117*(E12), E00H06. https://doi.org/10.1029/2011JE003951

Freed, A. M., Johnson, B. C., Blair, D. M., Melosh, H. J., Neumann, G. A., Phillips, R. J., et al. (2014). The formation of lunar mascon basins from impact to contemporary form. *Journal of Geophysical Research: Planets*, *119*(11), 2378–2397. https://doi.org/10.1002/2014je004657

Goossens, S., Genova, A., James, P. B., & Mazarico, E. (2022). Estimation of crust and lithospheric properties for mercury from high-resolution gravity and topography. *The Planetary Science Journal*, *3*(6), 145. https://doi.org/10.3847/psj/ac703f

Huang, Q., & Wieczorek, M. A. (2012). Density and porosity of the lunar crust from gravity and topography. *Journal of Geophysical Research*, *117*(E5), E05003. https://doi.org/10.1029/2012je004062

Johnson, B. C., Blair, D. M., Collins, G. S., Melosh, H. J., Freed, A. M., Taylor, G. J., et al. (2016). Formation of the orientale lunar multiring basin. *Science*, *354*(6311), 441–444. https://doi.org/10.1126/science.aag0518

Jolliff, B. L., Gillis, J. J., Haskin, L. A., Korotev, R. L., & Wieczorek, M. A. (2000). Major lunar crustal terranes: Surface expressions and crust-mantle origins. *Journal of Geophysical Research*, *105*(E2), 4197–4216. https://doi.org/10.1029/1999je001103

Kamata, S., Sugita, S., Abe, Y., Ishihara, Y., Harada, Y., Morota, T., et al. (2013). Viscoelastic deformation of lunar impact basins: Implications for heterogeneity in the deep crustal paleo-thermal state and radioactive element concentration. *Journal of Geophysical Research: Planets*, *118*(3), 398–415. https://doi.org/10.1002/jgre.20056

Kamata, S., Sugita, S., Abe, Y., Ishihara, Y., Harada, Y., Morota, T., et al. (2015). The relative timing of lunar magma ocean solidification and the late heavy bombardment inferred from highly degraded impact basin structures. *Icarus*, *250*, 492–503. https://doi.org/10.1016/j.icarus.2014.12.025

Karner, G. D., Studinger, M., & Bell, R. E. (2005). Gravity anomalies of sedimentary basins and their mechanical implications: Application to the Ross Sea Basins, West Antarctica. *Earth and Planetary Science Letters*, *235*(3), 577–596. https://doi.org/10.1016/j.epsl.2005.04.016

Lawlis, J. D. (1998). High temperature creep of synthetic olivine-enstatite aggregates (Doctoral dissertation). Pennsylvania State University. Retrieved from https://www.proquest.com/docview/304442834

Lompa, T., Ebbing, J., & Wünnemann, K. (2023). Replication data for: Evolution of impact basin gravity signatures on the lunar farside: A long-term alteration process (V4 ed.). TRR170-DB. https://doi.org/10.35003/BLEX70

Lompa, T., Wünnemann, K., Wahl, D., Padovan, S., & Miljković, K. (2021a). Numerical investigation of lunar basin formation constrained by gravity signature. *Journal of Geophysical Research: Planets*, *126*(11), e2021JE006908. https://doi.org/10.1029/2021JE006908

Lompa, T., Wünnemann, K., Wahl, D., Padovan, S., & Miljković, K. (2021b). Replication data for: Numerical investigation of lunar basin formation constrained by gravity signature (V4 ed.). TRR170-DB. https://doi.org/10.35003/mci3m3

Meinesz, F. A. V. (1939). Tables fondamentales pour la réduction isostatique régionale. *Bulletin Geodesique*, *63*(1), 711–776. https://doi.org/10.1007/BF03032435

Melosh, H. J. (2011). *Planetary surface processes*. Cambridge University Press. https://doi.org/10.1017/CBO9780511977848

Melosh, H. J., Freed, A. M., Johnson, B. C., Blair, D. M., Andrews-Hanna, J. C., Neumann, G. A., et al. (2013). The origin of lunar mascon basins. *Science*, *340*(6140), 1552–1555. https://doi.org/10.1126/science.1235768

Miljković, K., Collins, G. S., Wieczorek, M. A., Johnson, B. C., Soderblom, J. M., Neumann, G. A., & Zuber, M. T. (2016). Subsurface morphology and scaling of lunar impact basins. *Journal of Geophysical Research: Planets*, *121*(9), 1695–1712. https://doi.org/10.1002/2016je005038

Mohit, P. S., & Phillips, R. J. (2006). Viscoelastic evolution of lunar multiring basins. *Journal of Geophysical Research*, *111*(E12), E12001. https://doi.org/10.1029/2005je002654

Montesi, L. G. J. (2013). Solving the mascon mystery. *Science*, *340*(6140), 1535–1536. https://doi.org/10.1126/science.1238099

Morbidelli, A., Marchi, S., Bottke, W. F., & Kring, D. A. (2012). A sawtooth-like timeline for the first billion years of lunar bombardment. *Earth and Planetary Science Letters*, *355–356*, 144–151. https://doi.org/10.1016/j.epsl.2012.07.037

Morbidelli, A., Nesvorny, D., Laurenz, V., Marchi, S., Rubie, D. C., Elkins-Tanton, L., et al. (2018). The timeline of the lunar bombardment - Revisited. *Icarus*, *305*, 262–276. https://doi.org/10.1016/j.icarus.2017.12.046

Müller, M. (2007). *Information retrieval for music and motion* [Monograph]. Springer-Verlag Berlin Heidelberg. https://doi.org/10.1007/978-3-540-74048-3

Müller, M. (2015). *Fundamentals of music processing: Audio, analysis, algorithms, applications* (1st ed.). Springer International Publishing. https://doi.org/10.1007/978-3-319-21945-5

Nelson, D. M., Koeber, S. D., Daud, K., Robinson, M. S., Watters, T. R., Banks, M. E., & Williams, N. R. (2014). Mapping lunar maria extents and lobate scarps using LROC image products. In *45th Annual lunar and planetary science conference* (p. 2861).

Neumann, G. A., Zuber, M. T., Wieczorek, M. A., Head, J. W., Baker, D. M. H., Solomon, S. C., et al. (2015). Lunar impact basins revealed by gravity recovery and interior laboratory measurements. *Science Advances*, *1*(9), e1500852. https://doi.org/10.1126/sciadv.1500852

Orgel, C., Michael, G., Fassett, C. I., van der Bogert, C. H., Riedel, C., Kneissl, T., & Hiesinger, H. (2018). Ancient bombardment of the inner solar system: Reinvestigation of the "fingerprints" of different impactor populations on the lunar surface. *Journal of Geophysical Research: Planets*, *123*(3), 748–762. https://doi.org/10.1002/2017JE005451

Park, R. S., Konopliv, A. S., Yuan, D. N., Asmar, S., Watkins, M. M., Williams, J., et al. (2015). A high-resolution spherical harmonic degree 1500 lunar gravity field from the GRAIL mission. In *AGU fall meeting abstracts* (Vol. 2015, p. G41B-01).

Potter, R. W. K., Kring, D. A., Collins, G. S., Kiefer, W. S., & McGovern, P. J. (2013). Numerical modeling of the formation and structure of the orientale impact basin. *Journal of Geophysical Research: Planets*, *118*(5), 963–979. https://doi.org/10.1002/jgre.20080

Prettyman, T. H., Hagerty, J. J., Elphic, R. C., Feldman, W. C., Lawrence, D. J., McKinney, G. W., & Vaniman, D. T. (2006). Elemental composition of the lunar surface: Analysis of gamma ray spectroscopy data from lunar prospector. *Journal of Geophysical Research*, *111*(E12), E12007. https://doi.org/10.1029/2005je002656

Rybacki, E., & Dresen, G. (2000). Dislocation and diffusion creep of synthetic anorthite aggregates. *Journal of Geophysical Research*, *105*(B11), 26017–26036. https://doi.org/10.1029/2000JB900223

Smith, D. E., Zuber, M. T., Jackson, G. B., Cavanaugh, J. F., Neumann, G. A., Riris, H., et al. (2010). The lunar orbiter laser altimeter investigation on the lunar reconnaissance orbiter mission. *Space Science Reviews*, *150*(1), 209–241. https://doi.org/10.1007/s11214-009-9512-y

Solomon, S. C., Comer, R. P., & Head, J. W. (1982). The evolution of impact basins: Viscous relaxation of topographic relief. *Journal of Geophysical Research*, *87*(B5), 3975–3992. https://doi.org/10.1029/JB087iB05p03975

Spohn, T., Konrad, W., Breuer, D., & Ziethe, R. (2001). The longevity of lunar volcanism: Implications of thermal evolution calculations with 2D and 3D mantle convection models. *Icarus*, *149*(1), 54–65. https://doi.org/10.1006/icar.2000.6514

Stöffler, D., & Ryder, G. (2001). Stratigraphy and isotope ages of lunar geologic units: Chronological standard for the inner solar system. *Space Science Reviews*, *96*(1), 9–54. https://doi.org/10.1007/978-94-017-1035-0_2

Sugano, T., & Heki, K. (2004). Isostasy of the moon from high-resolution gravity and topography data: Implication for its thermal history. *Geophysical Research Letters*, *31*(24), L24703. https://doi.org/10.1029/2004GL022059

Tosi, N., Cadek, O., Behounková, M., Káňová, M., Plesa, A.-C., Grott, M., et al. (2015). Mercury's low-degree geoid and topography controlled by insolation-driven elastic deformation. *Geophysical Research Letters*, *42*(18), 7327–7335. https://doi.org/10.1002/2015GL065314

Turcotte, D. L., & Schubert, G. (2002). *Geodynamics*. Cambridge University Press. https://doi.org/10.1017/cbo9780511807442

Wahl, D., Wieczorek, M. A., Wünnemann, K., & Oberst, J. (2020). Crustal porosity of lunar impact basins. *Journal of Geophysical Research: Planets*, *125*(4), e2019JE006335. https://doi.org/10.1029/2019JE006335

Warren, P. H. (1985). The magma ocean concept and lunar evolution. *Annual Review of Earth and Planetary Sciences*, *13*(1), 201–240. https://doi.org/10.1146/annurev.ea.13.050185.001221

Watts, A. (2018). The use of object-oriented and process-oriented methods for gravity anomaly modelling of sedimentary basins. *Geophysical Journal International*, *215*(2), 1474–1482. https://doi.org/10.1093/gji/ggy353

Wessel, P., Luis, J., Uieda, L., Scharroo, R., Wobbe, F., Smith, W. H., & Tian, D. (2019). The generic mapping tools version 6. *Geochemistry, Geophysics, Geosystems*, *20*(11), 5556–5564. https://doi.org/10.1029/2019GC008515

Wieczorek, M. A. (2012). Grail crustal thickness archive. *Zenodo*. https://doi.org/10.5281/zenodo.997347

Wieczorek, M. A. (2015). 10.05 - Gravity and topography of the terrestrial planets. In G. Schubert (Ed.), *Treatise on geophysics* (2nd ed., pp. 153–193). Elsevier.

Wieczorek, M. A., & Meschede, M. (2018). Shtools: Tools for working with spherical harmonics. *Geochemistry, Geophysics, Geosystems*, *19*(8), 2574–2592. https://doi.org/10.1029/2018GC007529

Wieczorek, M. A., Meschede, M., Reinecke, M., Oshchepkov, I., de Andrade, E. S., Corbin, A., et al. (2022). Shtools/shtools: Version 4.10.1. *Zenodo*. https://doi.org/10.5281/zenodo.7064921

Wieczorek, M. A., Neumann, G. A., Nimmo, F., Kiefer, W. S., Taylor, G. J., Melosh, H. J., et al. (2013). The crust of the moon as seen by GRAIL. *Science*, *339*(6120), 671–675. https://doi.org/10.1126/science.1231530

Wilhelms, D. E., with sections by McCauley, J. F., & Trask, N. J. (1987). *The geologic history of the moon* (Tech. Rep.). U.S. Geological Survey. https://doi.org/10.3133/pp1348

Zhong, S. (1997). Dynamics of crustal compensation and its influences on crustal isostasy. *Journal of Geophysical Research*, *102*(B7), 15287–15299. https://doi.org/10.1029/97JB00956

Zhong, Z., Yan, J., Rodriguez, J. A. P., & Dohm, J. M. (2018). Ancient selenophysical structure of the Grimaldi basin: Constraints from GRAIL gravity and LOLA topography. *Icarus*, *309*, 411–421. https://doi.org/10.1016/j.icarus.2017.11.030

Zhong, Z., Yan, J.-G., Alexis, J., & Rodriguez, P. (2019). Ancient subsurface structure beneath crater clavius: Constraint by recent high-precision gravity and topography data. *Research in Astronomy and Astrophysics*, *19*(1), 009. https://doi.org/10.1088/1674-4527/19/1/9

Zhong, Z., Yan, J.-G., Zhang, T., Xiao, Z.-Y., & Rodriguez, J. A. P. (2019). Estimation of the elastic thickness over ancient mare moscoviense. *Research in Astronomy and Astrophysics*, *19*(12), 184. https://doi.org/10.1088/1674-4527/19/12/184

Zhu, M.-H., Wünnemann, K., & Potter, R. W. K. (2015). Numerical modeling of the ejecta distribution and formation of the orientale basin on the moon. *Journal of Geophysical Research: Planets*, *120*(12), 2118–2134. https://doi.org/10.1002/2015je004827

Zuber, M. T., Smith, D. E., Watkins, M. M., Asmar, S. W., Konopliv, A. S., Lemoine, F. G., et al. (2013). Gravity field of the moon from the gravity recovery and interior laboratory (GRAIL) mission. *Science*, *339*(6120), 668–671. https://doi.org/10.1126/science.1231507